Biomechanical origins of proprioceptive maps in the *Drosophila* leg

Akira Mamiya[1], Pralaksha Gurung[1], Igor Siwanowicz[2], Anne Sustar[1], Chenghao Chen[1,2], Jasper S. Phelps[3], Aaron T. Kuan[3], Alexandra Pacureanu[4], Wei-Chung Allen Lee[3, 5], Natasha Mhatre[6], John C. Tuthill[1]*

[1]Department of Physiology and Biophysics, University of Washington, WA, USA

[2]Janelia Research Campus, Howard Hughes Medical Institute, Ashburn, VA, USA

[3]Department of Neurobiology, Harvard Medical School, Boston, MA, USA

[4]ESRF, The European Synchrotron, Grenoble, France

[5]F.M. Kirby Neurobiology Center, Boston Children's Hospital, Harvard Medical School, Boston, MA, USA

[6]Department of Biology, Western University, London, Ontario, Canada

*Correspondence to tuthill@uw.edu

Abstract

Proprioception, the sense of body position and movement, is essential for effective motor control. Because proprioceptive sensory neurons are embedded in complex and dynamic tissues, it has been challenging to understand how they sense and encode mechanical stimuli. Here, we find that proprioceptor neurons in the *Drosophila* femur are organized into functional groups that are biomechanically specialized to detect features of tibia joint kinematics. The dendrites of position and vibration-tuned proprioceptors receive distinct mechanical signals via the *arculum*, an elegant mechanical structure that decomposes movement of the tibia joint into orthogonal components. The cell bodies of position-tuned proprioceptors form a *goniotopic* map of joint angle, whereas the dendrites of vibration-tuned proprioceptors form a *tonotopic* map of tibia vibration frequency. Our findings reveal biomechanical mechanisms that underlie proprioceptor feature selectivity and identify common organizational principles between proprioception and other topographically organized sensory systems.

Introduction

Flexible motor control of the arms and legs requires sensory feedback from proprioceptive sensory neurons (i.e., proprioceptors). Both invertebrate and vertebrate animals possess multiple subtypes of proprioceptors that detect unique aspects of limb position and movement (Tuthill and Azim, 2018). For example, in mammalian muscle spindles, Group Ia and II afferents encode muscle length and velocity (Macefield and Knellwolf, 2018). A functionally analogous structure in the insect leg, the femoral chordotonal organ (FeCO), monitors the kinematics of the femur/tibia joint (Field and Matheson, 1998; Krishnan and Sane, 2015). The FeCO of the fruit fly, *Drosophila melanogaster*, contains five subtypes of mechanosensory neurons with distinct stimulus feature selectivity and axonal projections (Mamiya et al., 2018): claw neurons encode tibia position (flexion or extension), hook neurons encode directional movement (flexion or extension), and club neurons encode bidirectional movement and low amplitude, high-frequency vibration (**Fig. 1**). Claw and hook neurons likely contribute to feedback control of leg movements, such as walking and grooming, while club neurons may be used to monitor vibrations in the external environment, such as detecting conspecific wingbeats during social interactions (Agrawal et al., 2020; Chen et al., 2021; McKelvey et al., 2021).

What mechanisms determine the feature selectivity of different proprioceptor subtypes? One possibility is that differences in intrinsic cellular properties, such as expression of specific mechanotransduction channels, allow different sensory neuron subtypes to sense distinct mechanical features. In mammals, muscle spindle sensory neurons sense mechanical forces using the Piezo2 channel (Nagel and Chesler, 2022), with possible contributions from DEG/ENaC channels (Bewick and Banks, 2021). Chordotonal neurons in *Drosophila* express Piezo, NompC, Iav, Nan, and Painless channels (Hehlert et al., 2021), although the distribution of these proteins across proprioceptor subtypes is not yet known.

An alternative mechanism for proprioceptor feature selectivity is biomechanical filtering. For example, specialized attachment structures could decompose and transmit distinct forces to different proprioceptor subtypes. Biomechanical force gradients could also give rise to topographic mapping of stimulus features, as in the vertebrate cochlea (Fettiplace and Fuchs, 1999) and invertebrate tympanal organ (Oldfield, 1982). However, the experimental inaccessibility of proprioceptive sensory organs, which are typically embedded deep within the body, have prevented investigation of their mechanical operation *in vivo*. Here, we investigate the relative contributions of mechanotransduction and biomechanics to proprioceptor feature selectivity in the *Drosophila* leg.

Results

Functional organization of the *Drosophila* Femoral Chordotonal Organ (FeCO)

We reconstructed the peripheral ultrastructure of the FeCO using an X-ray holographic nanotomography dataset of the *Drosophila* front leg (Kuan et al., 2020). We identified 152 total cell bodies in the FeCO, which are organized into three separate compartments called scoloparia (Field and Matheson, 1998) (**Fig. 1, Movies S1, S2**). We constructed split-Gal4 genetic driver lines that specifically label club, claw, and hook neurons (**Fig. 1C-D, S1, S2**) and compared fluorescence and

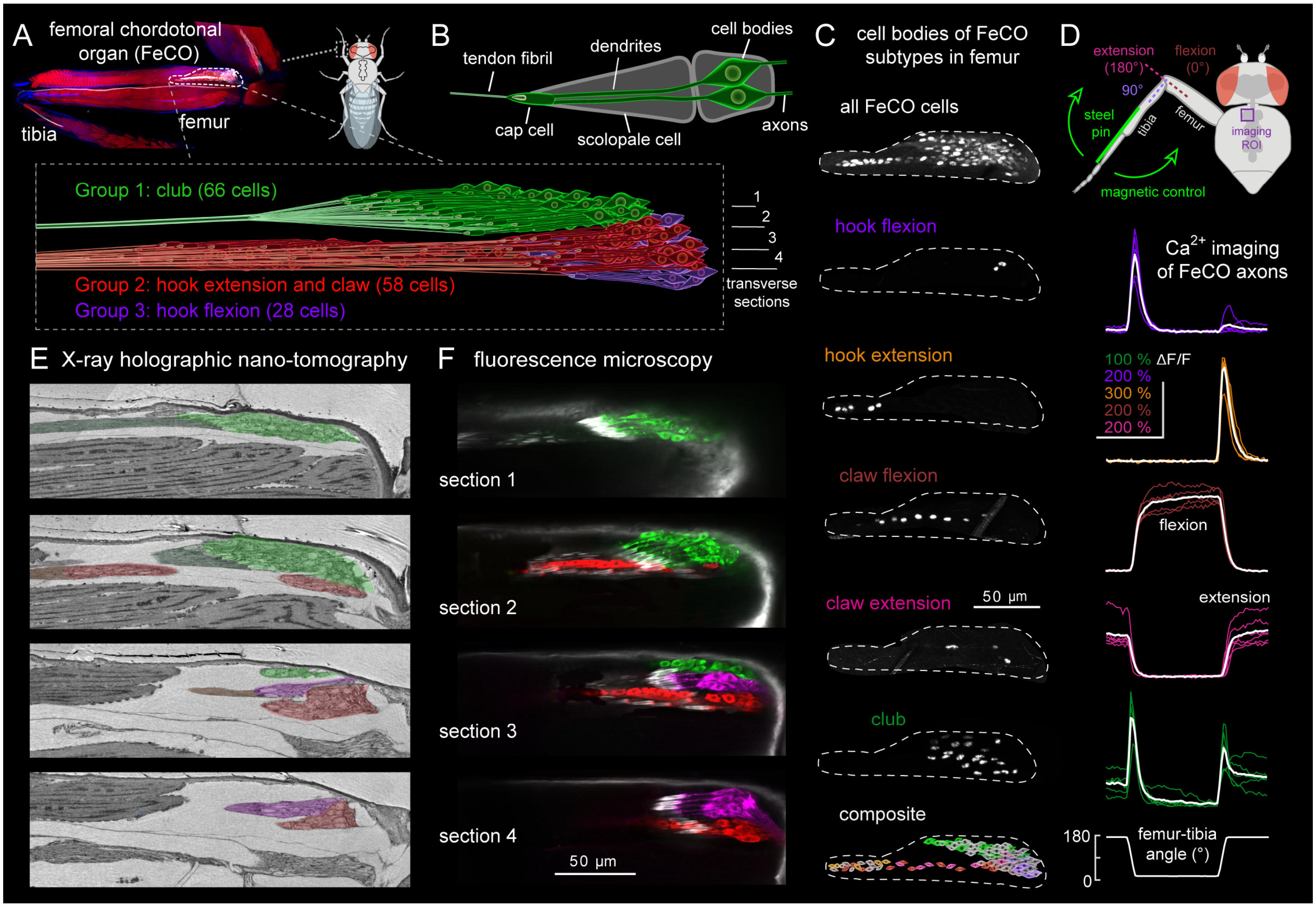

Fig. 1. Functional subtypes of FeCO proprioceptors are spatially clustered within three discrete compartments in the *Drosophila* leg. **(A)** Top: peripheral anatomy of the femoral chordotonal organ (FeCO, labeled with GFP driven by *iav-Gal4* (white); red is a phalloidin stain; blue is cuticle autofluorescence. Bottom: schematic of FeCO organization, based on X-ray reconstruction. **(B)** Dendrites of each pair of FeCO cells are surrounded by a scolopale cell that connect to a cap cell, which in turn connects to a tendon. (**C**) Split-Gal4 lines driving RFP label subtypes of FeCO cell bodies in specific locations in the femur. Bottom: a composite schematic showing the relative locations of cell bodies for each FeCO subtype. **(D)** Two-photon calcium imaging from axons of each FeCO subtype during controlled movements of the femur-tibia joint. Thin traces are from individual flies (n = 5-7) and the thick white line is the response average. **(E)** Reconstruction from an X-ray microscopy dataset of the fly femur reveals FeCO organization. Each image corresponds to a transverse section indicated in the schematic above. FeCO compartments and tendons are indicated by color shading. **(F)** The same image planes as **C** but visualized with confocal imaging (GFP driven by *iav-Gal4*; pseudo-colored to indicate compartment). Chordotonal cap cells are labeled with an antibody against phalloidin (white).

X-ray images to map the peripheral location of each FeCO subtype within the femur (**Fig. 1C, E-F**, **S1C-D**). We found that the largest and most dorsal compartment (Group 1) contains the club neurons, which encode tibia vibration and cyclic movement. Claw neurons, which encode the static angle of the femur-tibia joint, are distributed in a linear array along the long axis of the femur (Group 2). A smaller and more lateral compartment (Group 3) contains the hook flexion neurons, which respond transiently when the tibia flexes, but not during extension. The hook extension neurons, which respond transiently during tibia extension but not flexion, are located distal to the claw neurons in Group 2. Overall, our reconstruction revealed that FeCO neurons are organized into three functional compartments within the femur.

Mechanotransduction in FeCO proprioceptors

We next asked whether proprioceptors in the different FeCO compartments express different mechanotransduction channels, which could provide a mechanism for feature selectivity of club, hook, and claw neurons. We used driver lines to map the expression of eleven candidate mechanotransduction genes in the FeCO (**Fig. S3**). We found that each of three compartments contained cells expressing multiple different mechanotransduction channels (e.g., iav, nan, nompC, painless, Piezo, Piezo-like, and TMEM63). This heterogeneity is consistent with mechanosensory gene expression of putative FeCO neurons in a single-cell RNA-seq atlas of the *Drosophila* leg (**Fig. S3;** Li et al., 2022). Thus, differential expression of known mechanotransduction channels is not sufficient to account for feature selectivity of proprioceptor subtypes in the fly FeCO.

Biomechanical coupling of the FeCO and tibia

We next asked whether there exist biomechanical differences between proprioceptor subtypes. To understand how FeCO neurons are mechanically coupled to the tibia, we used the X-ray microscopy dataset to reconstruct their distal attachment structures (**Fig. 1E**). The ciliated dendrites of each pair of FeCO neurons are ensheathed in a scolopale cell that attaches to a sensory tendon via an actin-rich cap cell (**Fig. 1B**). Tracing the termination point of each cap cell allowed us to determine the tendon attachment of each FeCO neuron in the X-ray and fluorescence images (**Fig. 1E-F**). We found that the three different FeCO compartments attach to different tendons (**Fig. 2A**). The tendons connected to Groups 2 and 3 (claw and hook) merge and fuse ~100 μm distal to the FeCO, while the tendon connected to Group 1 (club) remained separate. The two primary tendons, which we refer to as medial and lateral, then converge upon a tooth-shaped structure in the distal femur (**Fig. 2A-C**). A similar structure was previously described in the beetle leg, where it was named the *arculum* (Frantsevich et al., 2019). In *Drosophila*, we found that the medial tendon attaches to the arculum's medial root, while the lateral tendon attaches to the arculum's lateral root (**Fig. 2A-C, Movie S3**). The arculum is then coupled to the base of the tibia-extensor tendon and to the tibia joint (**Fig. 2C**).

Our finding that different sensory neuron subtypes are attached to the tibia via different tendons points toward a biomechanical origin for differences in mechanical feature selectivity. We did not observe efferent innervation of the FeCO, nor did we see connections between the FeCO and surrounding tissues within the femur (e.g., muscles), as was reported in a previous study (Shanbhag et al., 1992). Overall, both our anatomical (**Fig. 1**) and physiological (**Fig. S3**) data support the conclusion that FeCO sensory neuron activity is determined by the mechanical forces transmitted from the tibia via the arculum. We therefore sought to understand how the different tendons transmit mechanical forces to FeCO sensory neurons during movements of the femur-tibia joint. We focused our analysis on the club and claw neurons because they attach to distinct tendons (lateral vs. medial), are selective for distinct kinematic features (vibration/movement vs. position), and we possess clean genetic driver lines that specifically label these cell populations (**Fig. 1C-D**).

The arculum decomposes and transmits distinct mechanical signals to the different FeCO compartments

We first investigated how mechanical forces are transmitted during small (< 1 μm), high frequency (100-1600 Hz) tibia vibrations; stimuli that excite club but not claw neurons (Mamiya et al., 2018). Because the lateral and medial tendons attach to different parts of the arculum (**Fig. 2A-C**), we focused on understanding how these two attachment points move during tibia vibration. Arculum movements during tibia vibration were too small to track *in vivo*, so we used a finite element model to investigate how the arculum responds to vibration (**Fig. 2D**). In the model, the arculum was suspended in the femur by four tendons (the tibia joint tendon, tibia extensor tendon, lateral FeCO tendon, and medial FeCO tendon) that were each modeled as springs. The attachment points of the tendons were not rigid, allowing the arculum to both rotate and translate. To simulate joint vibration, we applied a periodic linear force to the tibia joint tendon. The model predicted that the arculum rocks in response to tibia vibration, causing it to rotate slightly as the tibia oscillates. This rocking moves the lateral and medial roots of the arculum in different directions. Movements of the lateral root were larger along the long axis of the femur, while movements of the medial root were larger along the orthogonal axis (**Fig. 2D**). This result was consistent across a wide range of tibia vibration frequencies (**Fig. S4A**). The rocking of the medial root was also visible in bright-field imaging of the arculum during spontaneous leg movements (**Movie S4).**

Our model suggests that the arculum decomposes the linear movement of the tibia into two orthogonal vectors. A helpful analogy for this decomposition is a slider-crank linkage, which is used in engines to convert linear motion into rotatory motion (**Fig. 2E**). In the case of the arculum, the two movement vectors are then transmitted along two different tendons: the lateral FeCO tendon transmits on-axis movements to the dendrites of the club cells, while the medial FeCO tendon transmits primarily off-axis movements to the claw neurons, reducing on-axis movements by as much as 30x. This difference between the two tendons provides a potential mechanism for our prior observation that the amplitude threshold of claw neurons is more than 10 times higher than that of club neurons (Mamiya et al., 2018).

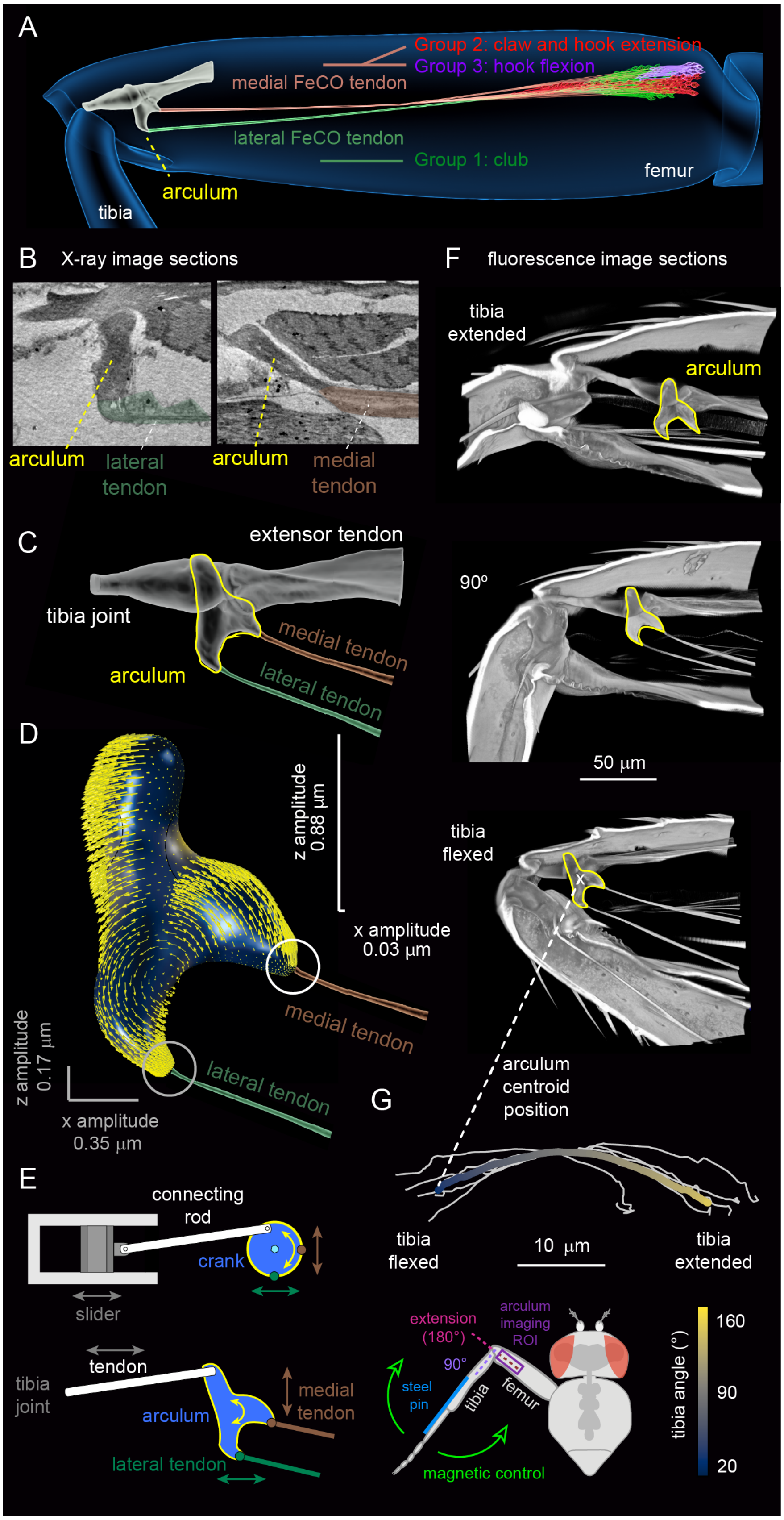

Fig. 2. The arculum decomposes and transmits distinct mechanical signals to different subtypes of FeCO sensory neurons. **(A)** FeCO neurons are mechanically coupled to the tibia via two sensory tendons that converge upon the arculum. **(B)** X-ray image sections showing how the lateral and medial tendons attach to the arculum. **(C)** The arculum and its tendons, segmented from a confocal image of the femur. **(D)** A 3D finite element model of the arculum, stimulated by low amplitude, periodic forces at its base (top). Yellow arrows represent the arculum movement during vibration; the arculum rotates and the attachment point for the medial tendon (right) moves mainly in the z direction, while the attachment point for the lateral tendon (bottom) moves in the x direction. **(E)** A schematic showing how linear motion is translated into rotation in a manner analogous to a slider-crank linkage. **(F)** Autofluorescence images of the arculum at different femur-tibia joint angles. As the tibia flexes, the arculum translates toward the femur/tibia joint. A white "x" marks the position of the arculum centroid that we tracked with *in vivo* imaging in G. **(G)** Measurements of arculum position during tibia flexion/extension with trans-cuticular two-photon imaging (setup schematized below). The plot above shows arculum centroid position during full tibia flexion (white lines; n = 6 flies). The thick colored line is the average trace (color indicates the tibia angle).

We next sought to understand how slower, nearly static, mechanical forces are transmitted to FeCO cells during larger changes in femur/tibia joint angle, such as those that occur during self-generated tibia movements like walking (Karashchuk et al., 2021). When the tibia flexes, the arculum translates distally toward the femur/tibia joint and moves laterally by a smaller distance (**Fig. 2F-G**). When the tibia extends, the arculum translates proximally, away from the femur/tibia joint. Thus, the primary effect of arculum translation is to pull/push the FeCO tendons along the long axis of the femur. This is consistent with our previous finding that large flexion/extension movements excite both claw and club neurons (Mamiya et al., 2018).

We took advantage of the autofluorescence of the arculum and FeCO tendons to visualize their movements during tibia flexion and extension with *in vivo* two- and three-photon imaging (**Fig. 2G**). The autofluorescence of the FeCO tendons was brighter under three-photon excitation (1300 nm). However, the faster repetition rate of the two-photon excitation laser (920 nm) was required to track arculum movements *in vivo* (**Fig. S4C, D**). Overall, our results from *in vivo* multiphoton imaging (**Fig. 2G)** were consistent with confocal images of the arculum in which the muscles and other soft tissues were digested for optical clarity (**Fig. 2F**). During tibia flexion, the arculum translates distally in a slightly curved trajectory that reaches a maximum point when the tibia is at 90° (**Fig. 2G**). In addition to these translational movements, the arculum also rotates slightly to be more perpendicular to the long axis of the femur as the tibia flexes (**Fig. S4B**). As the arculum translates, the FeCO tendons do not bend, indicating that they are stiff. Therefore, we conclude that movements of the tibia result in translation of the arculum and FeCO tendons, which alter the mechanical strain on proprioceptor dendrites.

A biomechanical model for joint angle selectivity among claw neurons

The mechanical forces at the FeCO cell dendrites depend not only on the movements of the tendons, but also on how the tendons interact with the cap cells and sensory neurons. To understand how claw cells are mechanically stimulated by joint movement, we simultaneously tracked the position of fluorescently labeled FeCO cell nuclei and cap cells using *in vivo* two-photon imaging, while slowly moving the tibia between flexion and extension (**Fig. 3A**). We found that both claw neurons and cap cells are mobile, translating distally when the tibia flexes and translating proximally when the tibia extends (**Fig. 3B, C**). In addition to the large movements along the distal-proximal axis of the femur, claw neurons and cap cells also translate slightly along the perpendicular axis (**Fig. 3B, Fig. S5**). We also noticed that the distance that claw cell bodies and cap cells translate during tibia flexion and extension increases linearly with their relative position along the proximal to distal axis of the femur (**Fig. 3E**). In other words, distal claw neurons and cap cells move farther than proximal cells for a given change in tibia angle (**Fig. 3E**). This relationship suggests the existence of a gradient of mechanical strain among claw neurons, which could provide a mechanism that allows different cells to respond to different tibia joint angles.

To investigate the strain distribution across the claw cell population, we constructed a series of finite element models based on the architecture of the FeCO and tendon attachments from the X-ray reconstruction (**Fig. 1**), as well as the movements of arculum (**Fig. 2**) during tibia flexion/extension. The model consisted of a series of coupled mechanical elements: claw cell bodies, dendrites, cap cells, tendon fibrils, the medial tendon, and the arculum (**Fig. 3D**). We modeled these elements as linear elastic materials and embedded them in elastic tissue mimicking the extracellular matrix surrounding the FeCO. We defined an equilibrium position in the model when the angle between the tibia and femur is 90°; this is the angle at which claw neuron activity is minimal (**Fig. S2**; Mamiya et al., 2018). We used the model to simulate how FeCO cells move (**Fig. 3F, S5**) and strain develops on the sensory neuron dendrites (**Fig. 3G-H**) as the tibia flexes and extends.

In addition to reproducing the major features of the claw and cap cell movements (**Fig. 3F, S5**), the model also predicted the existence of a spatial gradient of mechanical strain among claw neurons. Specifically, strain was higher for more proximal cells than more distal cells (**Fig. 3G-H**) and the gradient was steeper during tibia flexion than extension (**Fig. 3G-H**). If all claw neurons have similar sensitivity to mechanical strain, this gradient predicts proximal neurons will become active first as the tibia flexes, followed by more distal neurons. In other words, the model predicts a map of leg joint angle across the population of flexion-tuned claw neurons. It also predicts a similar but weaker joint angle map for extension-tuned claw neurons. We define a new term to describe this map: *goniotopic* (*gōnia* is the Greek word for angle).

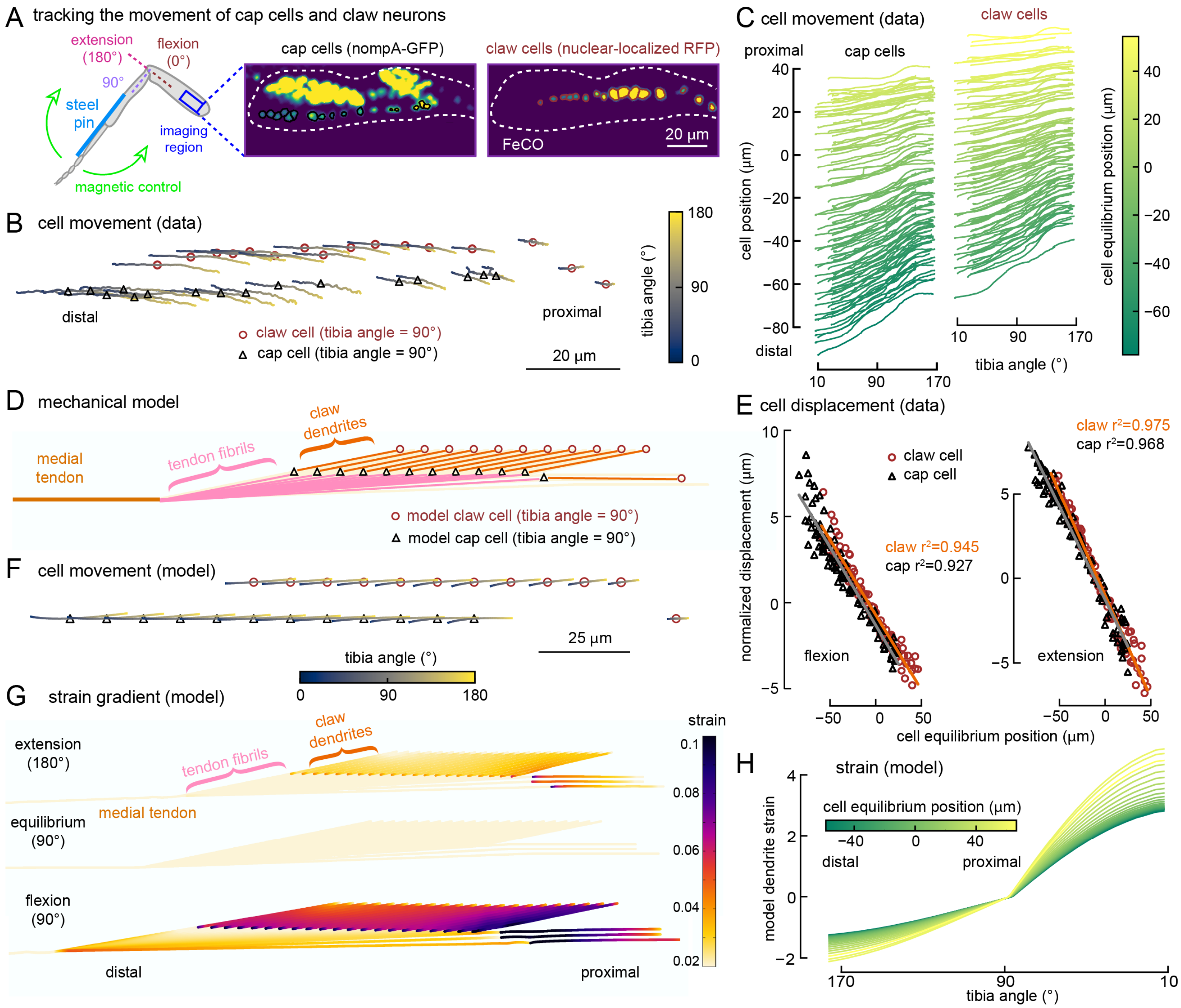

Fig. 3. A spatial gradient of cell movement and mechanical strain among position-tuned claw neurons. **(A)** We imaged RFP labeled claw cell nuclei and GFP labeled cap cells (each colored circle indicates the tracked cell) in the femur using transcuticular two-photon microscopy, while swinging the tibia from extension to flexion with a magnetic control system. (**B**) Example traces showing the position of claw cells (brown circles) and cap cells (grey triangles) during full tibia flexion. The color of each trace indicates tibia angle. (**C**) The position of cap cells (left) and claw cells (right) along the distal-proximal axis of the femur as the tibia moved from full extension to full flexion (n = 6 flies). We normalized the cell position within each fly by subtracting the average claw movement for each fly. **(D)** A finite element model of claw and cap cells. Model claw cells connect to the cap cells via their dendrites. The cap cells in turn connects to the medial tendon via tendon fibrils that fan out from the end of the medial tendon. Only 1/2 of the cells in the model are shown for display purposes. **(E)** Movement of claw and cap cells during tibia flexion (left) and extension (right) vs the cell's position along the distal to proximal axis of the femur (normalized as in **C**). (n = 6 flies). **(F)** Same as **C**, but for the movement of cells in the model. **(G)** A map of strain in the dendrites of model claw cells at different tibia angles. (**H**) The strain (1st principal invariant strain) in different claw dendrites plotted against the tibia angle. The dendrites stretched during tibia flexion (< ~90˚) and were compressed during tibia extension (> ~90˚). To emphasize the difference between the stretching and compression, we plotted the strain during compression as negative. The color of each line represents the cell equilibrium position along the distal-proximal axis of the femur.

A goniotopic map among claw proprioceptors in the fly leg

To test for the existence of a goniotopic map of leg joint angle among claw neurons, we measured the angular tuning of claw cell bodies inside the femur with volumetric two-photon calcium imaging. Imaging somatic GCaMP signals together with activity-independent tdTomato fluorescence allowed us to track individual cells and simultaneously measure neural activity, relative cell position, and claw cell movement (**Fig. 4A**). Consistent with the finite element model prediction, we found that flexion of the tibia first activated flexion-tuned claw neurons in the proximal FeCO, followed by the activation of increasingly distal cells at more acute angles (**Fig. 4A-C**). This goniotopic map was consistent across flies and different genetic driver lines labeling claw flexion neurons (**Fig. 4C-F**, **S6**).

We observed a similar, though less robust, goniotopic map within the extension-tuned claw cells (**Fig. S6)**. However, contrary to the prediction of the model, extension of the tibia first activated the more distal claw extension cells, followed by activation of the more proximal cells as the tibia angle increased further (**Fig. S6**). The difference in the orientation of the goniotopic map between our model and experimental data suggests that claw flexion and extension neurons may sense different mechanical parameters; for example, claw-extension neurons may detect decreases in strain or increases in strain along an orthogonal axis.

What properties of the FeCO are important for establishing the gradient of cell movement and mechanical strain among claw cells? By modifying different components of the model (**Fig. S7**), we found that the orientation of the fibrils that connect the FeCO cap cells to the medial tendon was critical to the establishment of the goniotopic map (**Fig. S7B**). Because the fibrils fan out from a single endpoint of the medial tendon, the fibrils that connect to more proximal claw cells are oriented more parallel to the direction of tendon movement, while those that connect to more distal claw cells are more perpendicular (**Fig. 3D**). When the tendon is pulled towards the joint during the tibia flexion, the fibrils connected to more proximal cells transfer most of the force in a direction that stretches the proprioceptor dendrites and increases the strain in these cells. Because proximal claw cells receive a smaller proportion of the overall force, their cell bodies also translate less.

In summary, our measurements of claw cell movement and calcium activity reveal a topographic map of joint angle across the linear array of claw neurons. Proximal claw cells are active at more obtuse angles during tibia flexion, and distal claw cells are active at more acute angles. Combined with the model predictions of an equivalent map of strain accumulation, these results point to a biomechanical origin for joint position tuning and the goniotopic map among claw neurons.

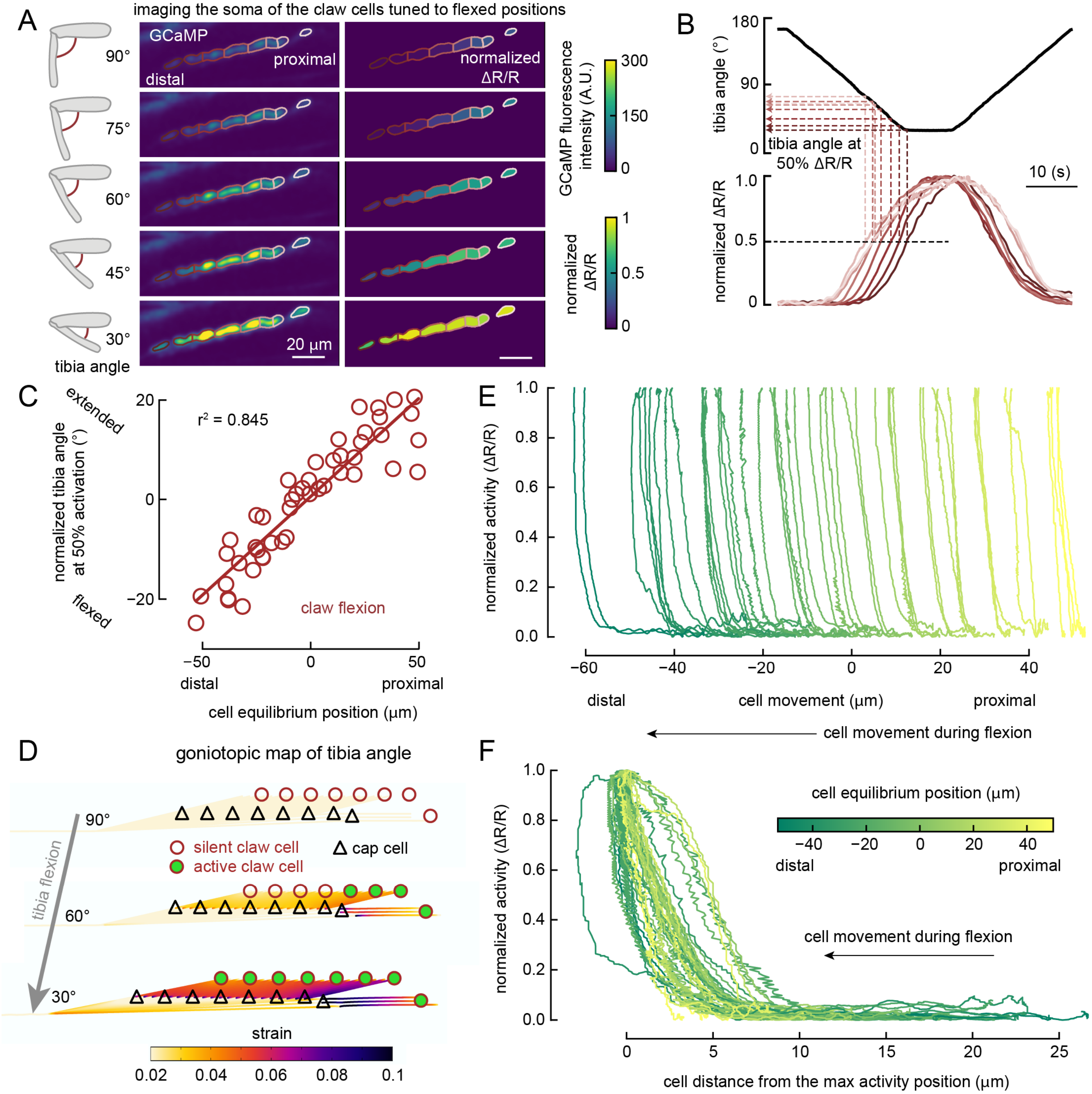

Fig. 4. A goniotopic map of tibia joint angle among claw neurons. **(A)** Example images of GCaMP7f fluorescence (left column) and normalized activity (right column) of flexion-selective claw neurons during slow tibia flexion (6°/s) recorded with two photon microscopy. Each colored circle indicates a tracked cell. Claw cell bodies move distally and increase their calcium activity as the tibia flexes. (**B**) Tibia angle (top) and normalized calcium activity (bottom) during the example recording shown in **A**, indicating the tibia angle where each cell reached 50% of its peak activity. The color scheme is the same as in **A**. More distal cells (darker shades of copper) reached 50% of their peak activity at more acute angles. (**C**) A linear relationship between each claw cell's position along the proximal-distal axis of the femur and the tibia angle when the cell reached 50% of its maximum activity. Within each fly, we normalized the tibia angle at which cells reached their 50% maximum activity (see Methods for details). (**D**) Schematic illustrating how the goniotopic map of tibia angle is represented by the activity of the flexion selective claw cells. **(E)** Normalized activity (ΔR/R) of the flexion selective claw cells (same data as shown in **C**; 47 cells from 7 flies) as the cells moved along the proximal-distal axis of the femur during flexion. For each cell, we plotted the activation curve starting from the beginning of the flexion (most proximal position for that cell) until a point where it reached maximum activation. The color of each line represents the cell's equilibrium position along the distal-proximal axis of the femur (color map shown in **F**). **(F)** Same traces as in **E**, but each trace is aligned to the position of the cell where it reached maximum activity. The shape of the activation curve is similar across cells.

A tonotopic map of tibia vibration frequency among club neuron dendrites

Finally, we investigated whether a topographic map exists among club neurons. Unlike claw neurons, which translate within the femur as the tibia flexes and extends, club neurons move very little (< 2 µm; **Fig. S8**), indicating that their cell bodies are anchored to the leg cuticle. Anchoring cell bodies may contribute to club neuron sensitivity by increasing mechanical strain between club cells and the tendon during tibia movement.

To test for the presence of a tonotopic map within the FeCO, we vibrated the tibia at different frequencies (100-1600 Hz; 0.9 µm amplitude) and recorded calcium activity from club neurons in the femur with two-photon imaging (**Fig. 5A**). During vibration, we saw consistent increases in intracellular calcium in the dendrites of the club neurons (**Fig. 5B-C**). As we increased the vibration frequency, the response amplitude increased and reached a plateau around 800 Hz (**Fig. 5C**). In addition to the increase in response amplitude, we also observed a shift in the spatial distribution of calcium activity (**Fig. 5B, D**). As the vibration frequency increased (200-1600 Hz), the center of the response moved from the distal/lateral side of the FeCO to the proximal/medial side (**Fig. 5B, D**). This shift was consistent and statistically significant across flies (**Fig. 5D, S9**). Thus, the FeCO also contains a tonopic map of tibia vibration frequency within the dendrites of the club neurons.

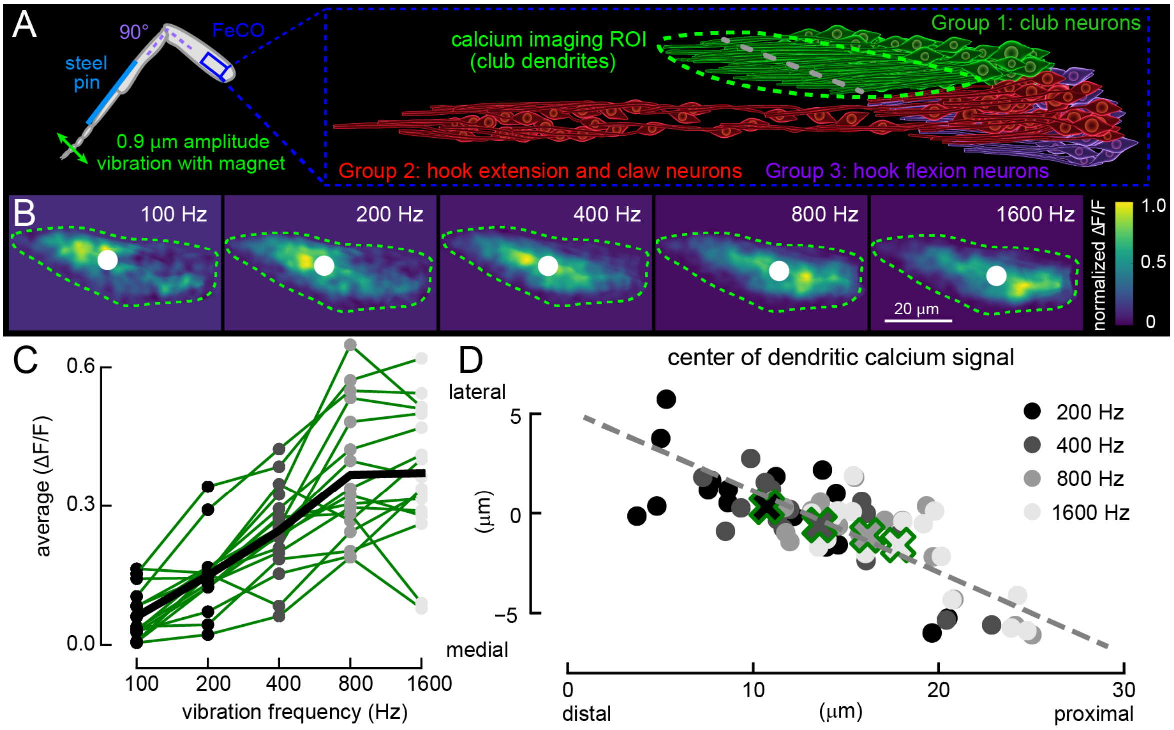

Fig. 5. A tonotopic map of tibia vibration frequency among club neurons. **(A)** Schematic of calcium imaging from the club neuron dendrites during tibia vibration using transcuticular two-photon microscopy (left). **(B)** Examples of calcium activity (ΔF/F, normalized for visualization) in the club dendrites during vibration of the tibia. White circles represent the weighted center of the calcium activity. Green dotted lines show ROI of club dendrites. **(C)** Average calcium activity (ΔF/F) in the club dendrites of individual flies (n= 17 flies) during the vibration of the tibia at different frequencies. Circles and thin lines are from individual flies and the thick black line represents the average across flies. **(D)** A scatter plot showing the weighted center of calcium activity for each vibration frequency (200 to 1600 Hz; n = 17 flies). Larger X's with green outlines indicate averages. The gray line shows the best-fit for the response centers and is also indicated in **A** to illustrate the primary spatial axis of the tonotopic map.

Discussion

The name *chordotonal* was originally coined by Vitus Graber in the 19th century, based on his observation of cells that resemble a bundle of chords under tension (Graber, 1881). However, it was previously unclear how the *chords* (i.e., tendons) were related to the mechanical tuning of sensory neurons in the *Drosophila* FeCO. Here, we describe two biomechanical mechanisms that allow specific subtypes of FeCO proprioceptors (**Fig. 1**) to detect distinct joint kinematic features.

First, tibia joint movement is split into the movements of two tendons by the arculum (**Fig. 2**). The two tendons move similarly for large amplitude, low frequency changes in tibia angle, such as those that occur when a fly walks. However, during small, high frequency vibrations of the tibia, the shape of the arculum allows it to push and pull the lateral tendon in a direction that excites the club sensory neurons, while moving the medial tendon in a perpendicular direction that does not excite the claw sensory neurons.

Second, we found that for claw neurons, distal cell bodies translate more during tibia flexion/extension compared to proximal cell bodies (**Fig. 3**). A finite element model based on the ultrastructure of the fly leg reproduced this relationship and further predicted that the mechanical strain on the claw dendrites is higher on proximal cells compared to distal cells resulting in a topographic representation of joint angle among claw neurons. Recordings of calcium signals from flexion-tuned claw neurons confirmed the presence of this goniotopic map of leg joint angle in the FeCO (**Fig. 4**). Further analysis of the finite element model revealed that the gradient in the angle of the medial tendon fibrils is critical for establishing the gradient of strain in the claw neuron dendrites **(Fig. S8).**

How is the tonotopic map in the dendrites of the club neurons (**Fig. 5**) generated? One possibility we considered is that the difference in the length of the tendon connected to each club cell could produce a different resonant frequency for each cell. However, a simple mechanical model based on measurements of the tendon fibrils from the X-ray microscopy data did not support this hypothesis: neither the longitudinal nor transverse vibrational modes would be sufficiently different to produce large enough changes in resonance at the club neuron dendrites. Another possibility is that systematic differences in the stiffness of each club neuron dendrite or in the mass of the cap cell could underlie their frequency tuning, similar to the situation in katydid hearing organs (Hummel et al., 2017). Finally, the tonotopic map could be established through tuning based on electrical resonance within club neurons, as occurs within the vertebrate cochlea (Fettiplace and Fuchs, 1999).

Topographic neural maps are found throughout the animal kingdom, including in other peripheral mechanosensory organs. For example, hair cells in the vertebrate cochlea (Fettiplace and Fuchs, 1999) and chordotonal neurons in the grasshopper tympanal organ (Oldfield, 1982) are organized into tonotopic maps of auditory frequency, similar to club neurons in the FeCO. Fractionation of the tibia joint angle range across position-tuned proprioceptors has been previously described in the grasshopper FeCO (Field, 1991; Matheson, 1992). Translation of FeCO cell bodies during limb movements has also been observed in other insects (Nishino and Sakai, 1997; Nishino et al., 2016). However, to our knowledge, goniotopic maps have not been described previously, perhaps due to the difficulty of recording activity from populations of mobile proprioceptive sensory neurons embedded within the body. Our findings raise the possibility that goniotopic maps of proprioceptive stimuli may exist in other organisms and sensory organs, thus creating a scaffold for a central topographic representation of the body.

Are the maps established in the fly leg preserved within central circuits? Similar to the tonotopic map we describe here among club neurons, there exists a map of vibration frequency among club axons in the VNC (Mamiya et al., 2018). Downstream VNC interneurons are also tuned to specific frequency ranges, indicating that they sample selectively from the topographic projections of club axons (Agrawal et al., 2020). In comparison, calcium imaging from position-tuned axons failed to resolve any topographic organization (Mamiya et al., 2018). However, interneurons downstream of claw axons encode specific joint angle ranges (Agrawal et al., 2020; Chen et al., 2021), suggesting that the goniotopic map may be preserved at the level of connectivity. Elucidating this organization will require reconstruction at the synaptic level, for example using connectomics of VNC circuits (Phelps et al., 2021).

Acknowledgements

We thank members of the Tuthill laboratory for technical assistance and feedback on the manuscript, particularly Ellen Lesser, who initially observed that FeCO neurons move within the leg, and Tony Azevedo, who was involved with the initial identification of the arculum within the X-ray microscopy dataset. We thank Thedita Pedersen for reconstructing FeCO neurons and dendrites from the X-ray microscopy dataset. We thank Katie Stanchak and Bing Brunton for discussions and helpful comments on the manuscript. We thank Rachel Wong, Gwyneth Card for generous sharing of equipment, and Jack Waters and Kevin Takasaki for construction of the 3-photon microscope. We thank Bertil Hille for suggesting the term *goniotopic*. We used stocks obtained from the Bloomington *Drosophila* Stock Center (NIH P40OD018537). We acknowledge support from the NIH (S10 OD016240) to the Keck Imaging Center at UW, and the assistance of its manager, Nathaniel Peters. This work was supported by a UW Innovation Award, a Searle Scholar Award, a Klingenstein-Simons Fellowship, a Pew Biomedical Scholar Award, a McKnight Scholar Award, a Sloan Research Fellowship, the New York Stem Cell Foundation, and NIH grants R01NS102333 and U01NS115585 to JCT. JCT is a New York Stem Cell Foundation – Robertson Investigator.

Author contributions

Conceptualization, A.M., P.G., N.M., and J.C.T; Methodology, A.M., P.G., I.S., J.S.P., A.S., A.P., A.K., N.M.; Investigation, A.M., P.G., I.S., J.S.P., A.S., N.M.; Resources, C.C., J.S.P, A.P., A.K, and W.A.L.; Analysis, A.M., P.G, I.S., A.S., N.M., J.C.T..; Writing, A.M., N.M., J.C.T.; Supervision, W.A.L., N.M., and J.C.T.; Funding Acquisition: W.A.L., N.M., and J.C.T.

Supplemental Figures

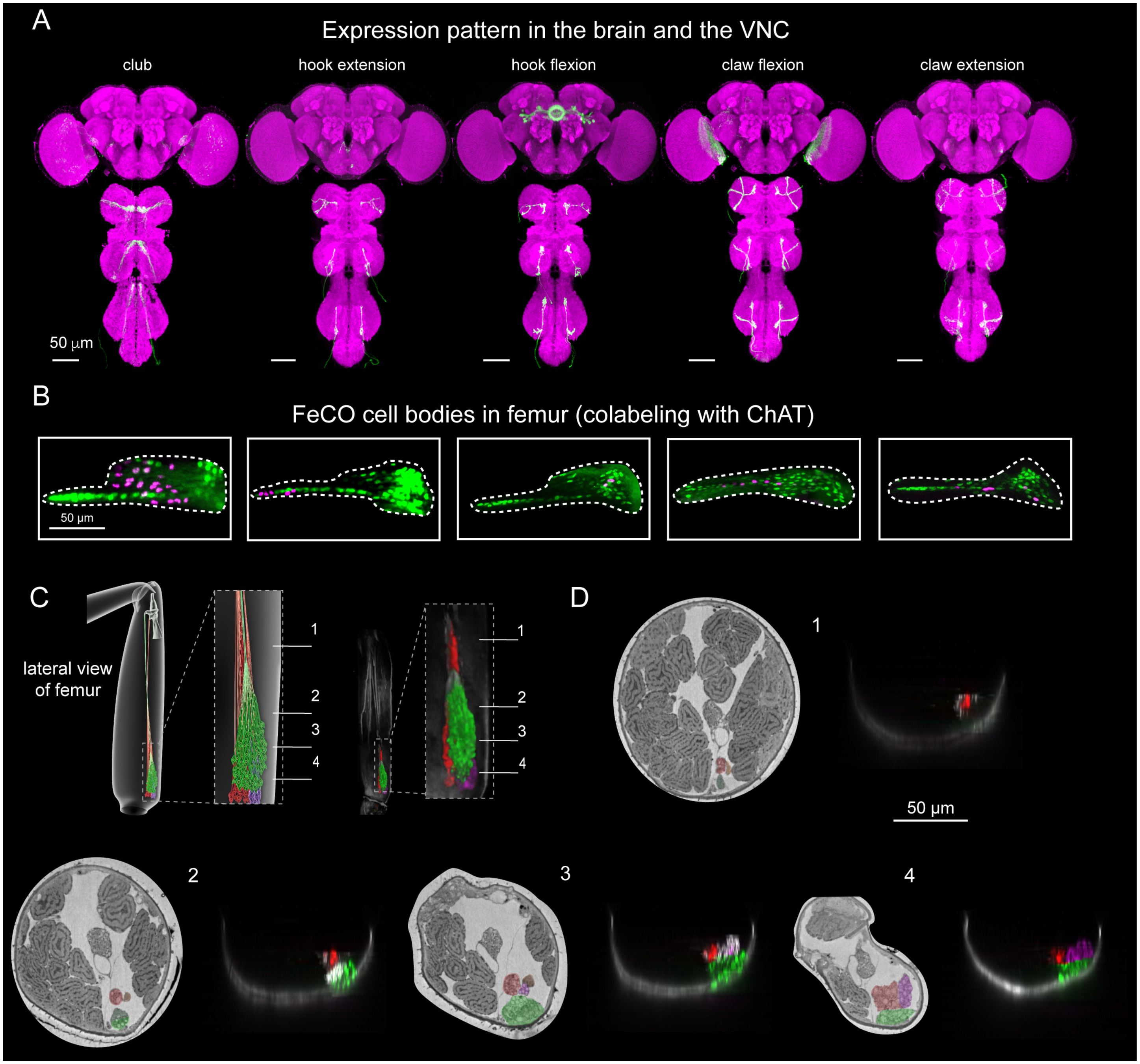

Fig S1. Proprioceptor subtypes are organized into functional compartments within the fly femur. **(A)** Confocal images of the fly brain and the VNC, showing the expression patterns of split-Gal4 drivers used to label specific subtypes of FeCO neurons (green; genotype listed in supplemental table 1). Magenta is a neuropil stain (nc82). **(B)** Confocal images of the FeCO cell bodies in femur, showing the expression pattern of Gal4 drivers used to label specific subsets of FeCO neurons (magenta). Green represents the expression pattern of ChAT-Gal4, which labels all mechanosensory neurons. **(C)** Same as Fig **1D**, but for cross sections of the femur. (**D**) Reconstruction of FeCO compartments from X-ray and confocal imaging of the fly femur. Each image corresponds to a transverse section indicated in the schematic in **C**. FeCO compartments and tendons are indicated by color shading.

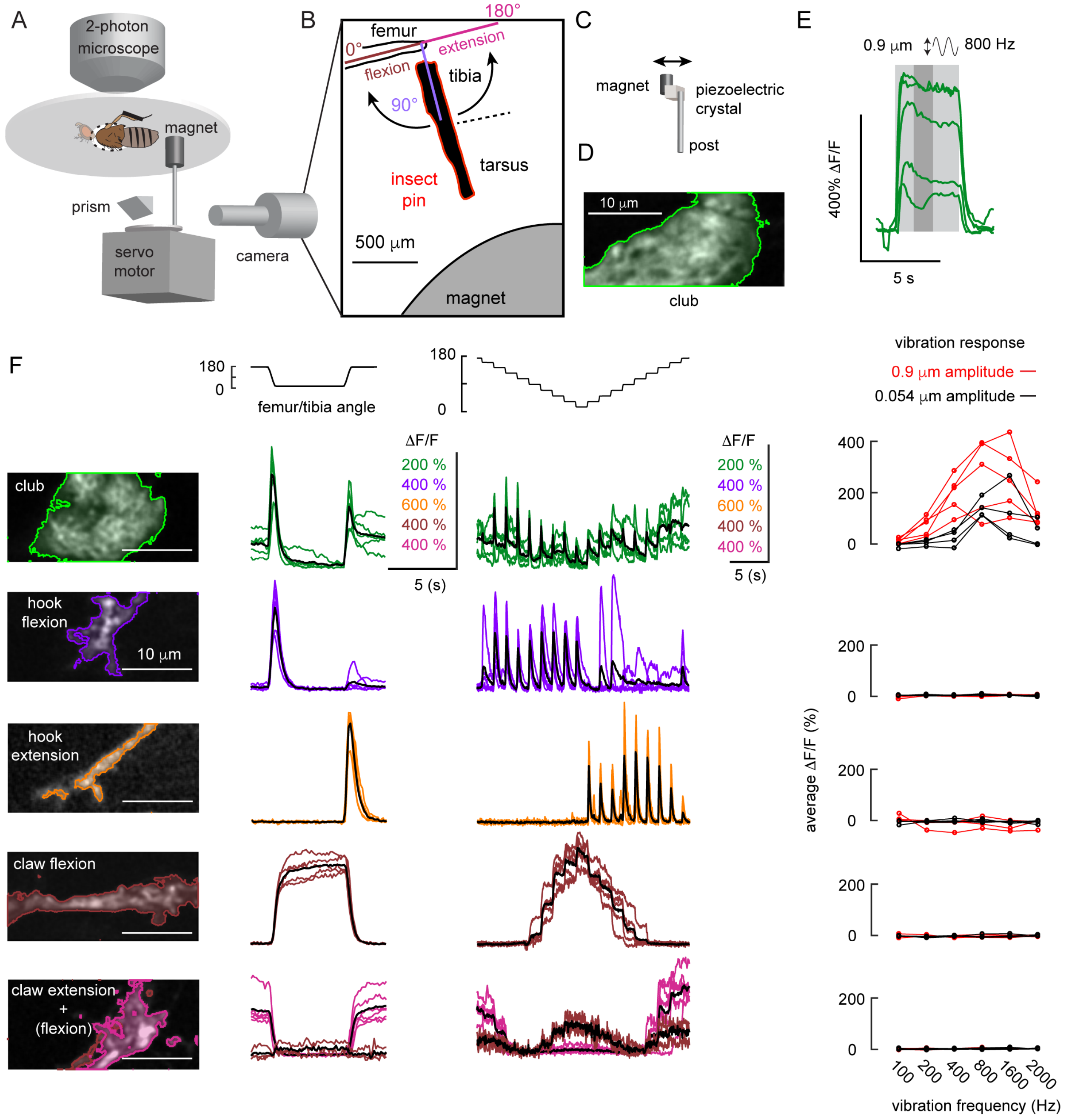

Fig S2. Calcium imaging from axons of FeCO split-Gal4 lines. **(A)** An experimental setup for two-photon calcium imaging from the axons of different types of FeCO neurons in the VNC while changing the femur-tibia joint angle. We controlled the joint angle by gluing a pin to the tibia and positioned it using a magnet mounted on a servo motor. We backlit the tibia with an IR LED and used a prism to record the view from the bottom with high-speed video camera. **(B)** An example frame from a video used to track joint angle. We painted the pin black to enhance the contrast against the bright background. **(C)** An experimental setup for vibrating the tibia with a magnet attached to a piezoelectric crystal. **(D)** An example two-photon image of the club axon terminal where we recorded the responses to the vibration stimuli (region of interest shaded with light green and surrounded by a green line). **(E)** Time courses of the club neuron's response (ΔF/F) to an 800 Hz, 0.9 μm vibration of the magnet (n = 5 flies). Each line represents the response from one fly. We averaged the activity in a 1.25 s window (indicated by a dark gray shading) starting from 1.25 s after the stimulation onset and used it as a measure of response amplitude in the rightmost column of F. **(F)** Calcium responses (ΔF/F) of the axons of different subsets of FeCO neurons to swing (2nd column), ramp-and-hold (3rd column), and vibration (4th column) stimuli. 1st column shows the GCaMP fluorescence of the axons of different subsets of FeCO neurons. 1st row: club (n = 5 flies), 2nd row: hook flexion (n= 5 flies), 3rd row: hook extension (n = 5 flies), 4th row: claw flexion (n= 5 flies), 5th row: claw extension and flexion (n= 6 flies). Because the Gal4 line for the 5th row contained a small number of flexion selective claw neurons in addition to the extension selective claw neurons, we separated the pixels into two clusters based on their response similarity to the swing or ramp-and-hold stimuli using k-means clustering. Each trace is the average response from one fly.

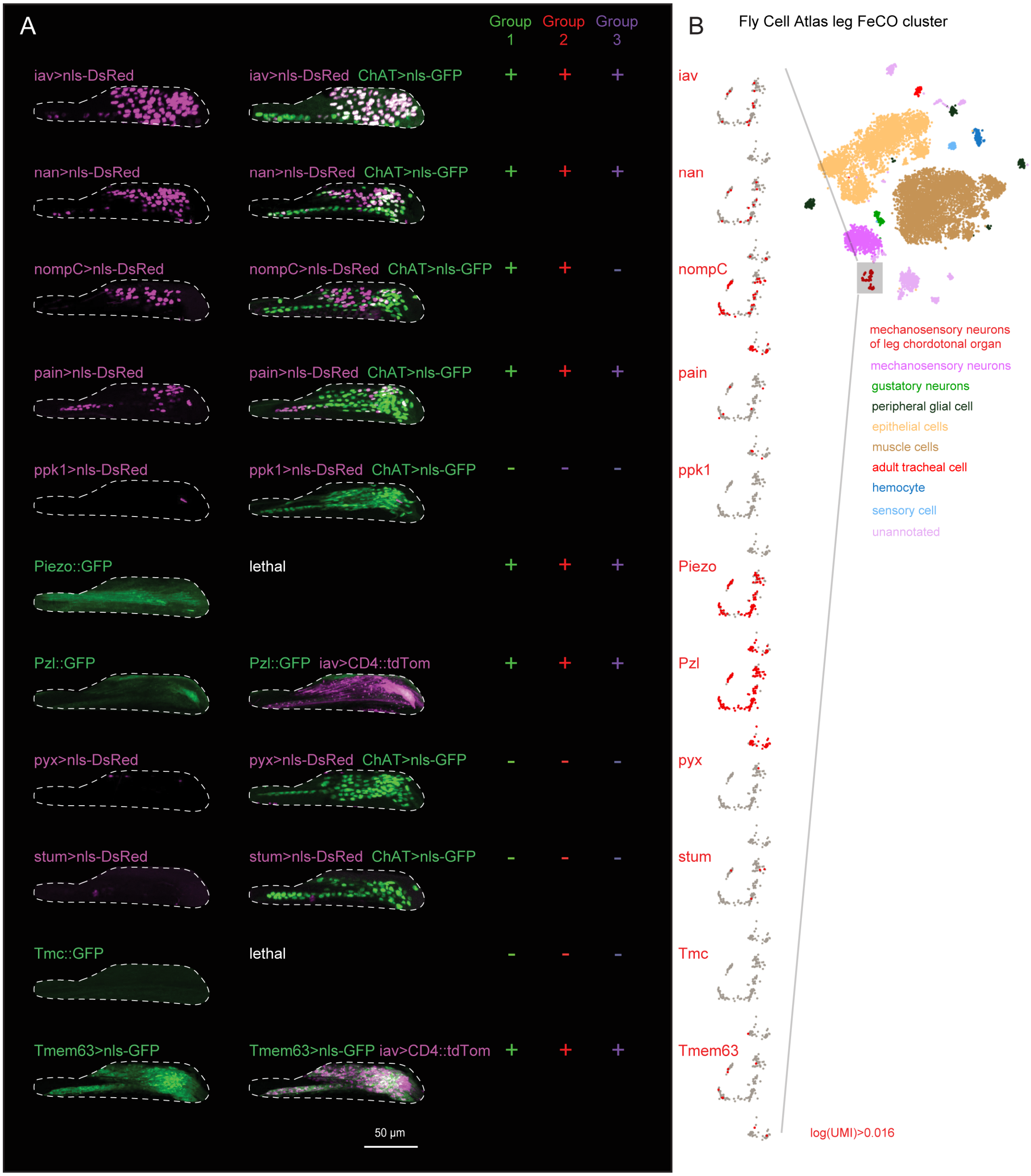

Fig. S3. Mechanotransduction channel expression in the femoral chordotonal organ (FeCO). **(A)** Confocal images of mechanotransduction channel reporter expression in the FeCO cell bodies in the femur. Images are co-labeled with either ChAT-Gal4 (labels all mechanosensory neurons) or iav-Gal4 (labels most FeCO cell bodies). In some cases, co-labeled genotypes are lethal and not shown. (+) and (-) indicate expression within scoloparia groups 1, 2, and 3. **(B)** Same genes as in **A**, RNA transcript expression from the Fly Cell Atlas leg dataset (Li et el., 2022). The "mechanosensory neuron of leg chordotonal organ" cluster is shown for each gene. This cluster contains 210 cells (grey or red dots). Red dots indicate transcript expression with a threshold log(UMI)>0.016. Screenshots from https://scope.aertslab.org FlyCellAtlas, 10x, Leg, Stringent dataset.

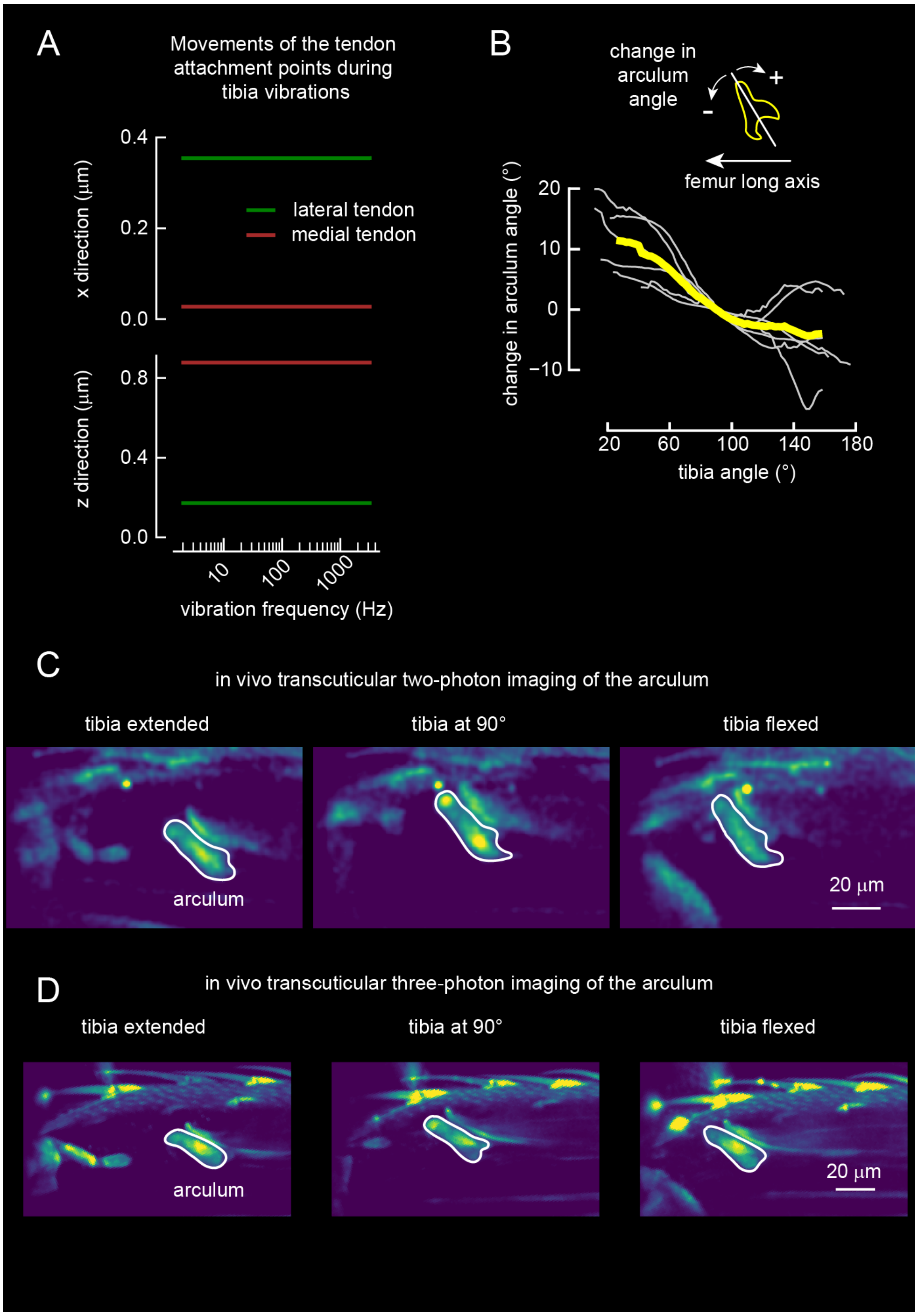

Fig. S4. Movements of the arculum during tibia vibration and flexion/extension. (**A**) Plots showing how the attachment point for the lateral (green line) and the medial (brown line) tendon moves in the x (top) and z (bottom) direction in a 3D finite element model of the arculum receiving small periodic forces at different frequencies (1-3000 Hz). (**B**) A plot showing the change in arculum angle during full tibia flexion. The change in arculum angle is measured as the difference from the arculum angle when tibia angle is at 90˚, and clockwise rotation is defined as positive change in the angle. (**C**) *in vivo* transcuticular two-photon images of the arculum at different tibia angles. White outline indicates the location of the arculum. (**D**) *in vivo* transcuticular three-photon images of the arculum at different tibia angles. White outline indicates the location of the arculum.

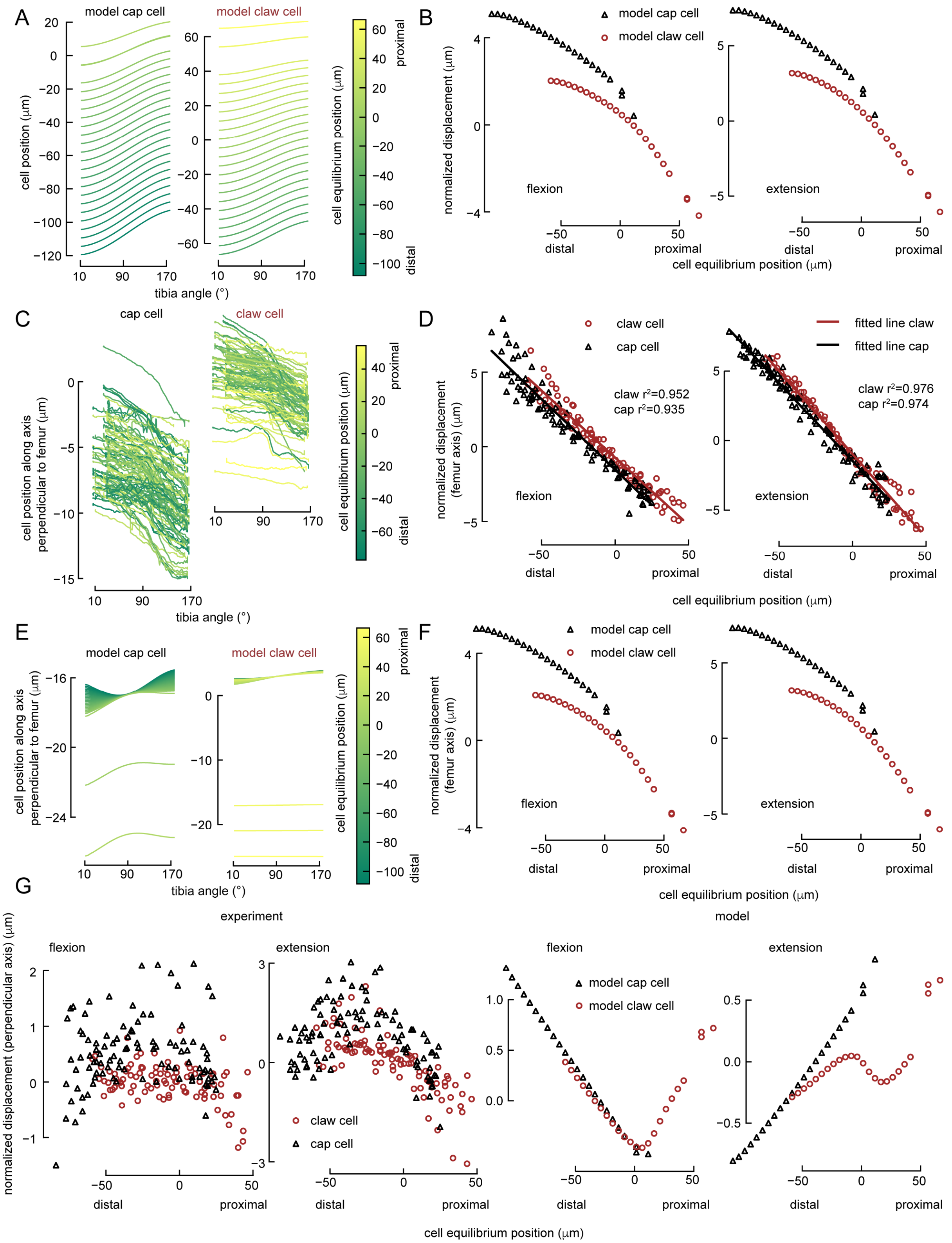

Fig S5. Further quantification of movements of the claw and cap cells during tibia flexion/extension for experimental and model data (same dataset and model as shown in **Fig. 3**). (**A**) Same as **Fig. 3C**, but for the model claw and cap cells. (**B**) Same as **Fig. 3E**, but for the model claw and cap cells. (**C**) Same as **Fig. 3C**, but for movements along the axis perpendicular to the long axis of the femur. **(D)** Same as **Fig. 3E**, but for the displacement distance along the long axis of the femur. **(E)** Same as **3C**, but for the model claw and cap cells. **(F)** Same as **3E**, but for the model claw and cap cells. **(G) 1st and 2nd columns**: Same as **D**, but for the displacement distance along the axis perpendicular to the distal-proximal axis of the femur. **3rd and 4th columns**: Same as the **1st and 2nd columns**, but for the model claw and cap cells.

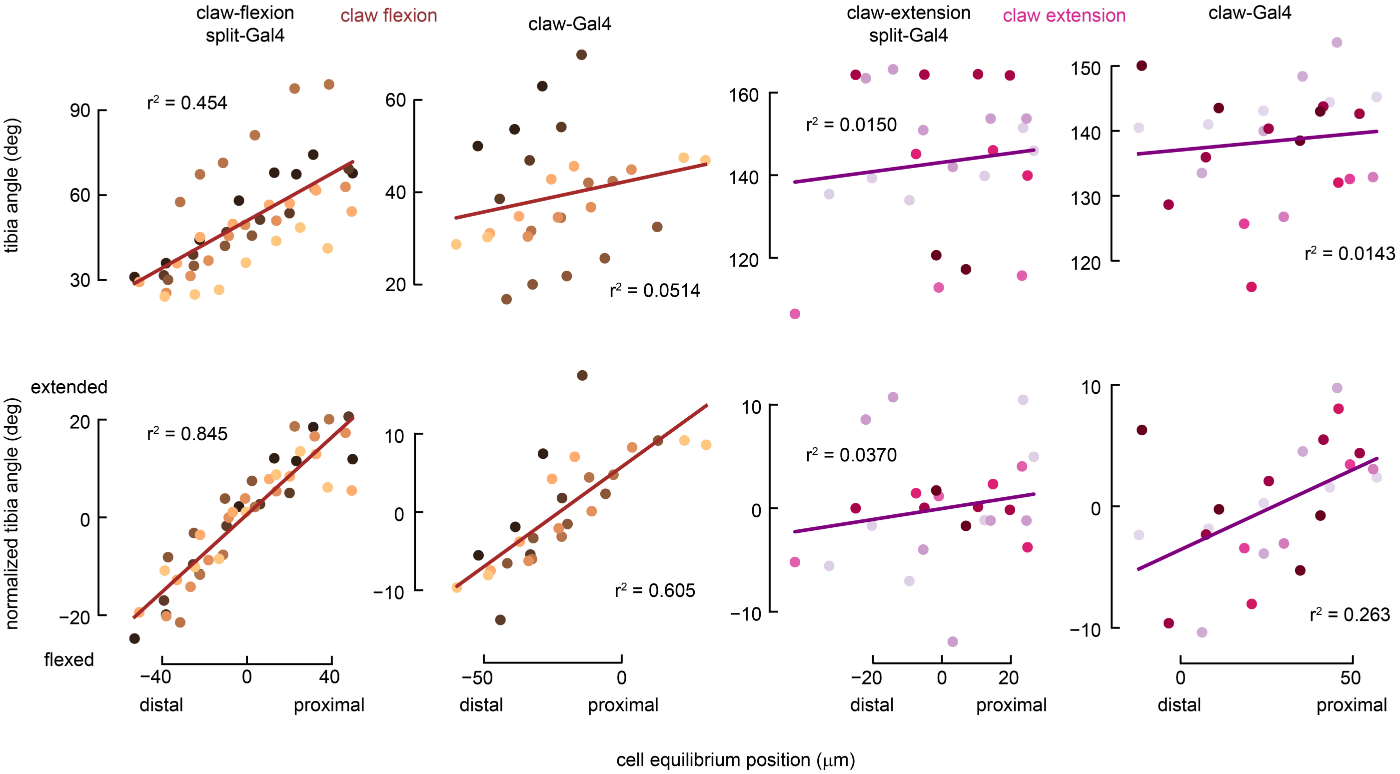

Fig S6. Further quantification of the relationship between the claw cells' positions and tuning to tibia angle (**Fig. 4**). **Top row:** Scatter plots showing the relationship between each cell's equilibrium position along the proximal-distal axis of the femur and the tibia angle when the cell reached 50% of its maximum activity during a slow tibia swing (6 °/s) from the flexed (**left two columns**) or extended (**right two columns**) side. We labeled flexion selective claw neurons (**1st and 2nd column**) with two different driver lines, claw-flexion split-Gal4 line (**1st column**, 7 flies; the same data as shown in **Fig. 4C**) or claw-Gal4 line (GMR73D10-Gal4; **2nd** column, 7 flies). We labeled extension selective claw neurons (**3rd and 4th column**) with claw-extension split-Gal4 line (**3rd column**, 6 flies) or claw-Gal4 line (GMR73D10-Gal4; **4th column**, 7 flies). Circles with different colors represent claw cells from different flies. The lines represent linear regression line. **Bottom row:** Same data as shown on the **top row**, but we normalized the tibia angle where the cells reached their 50% maximum activity by defining the average of this angle for all cells in each fly to be zero.

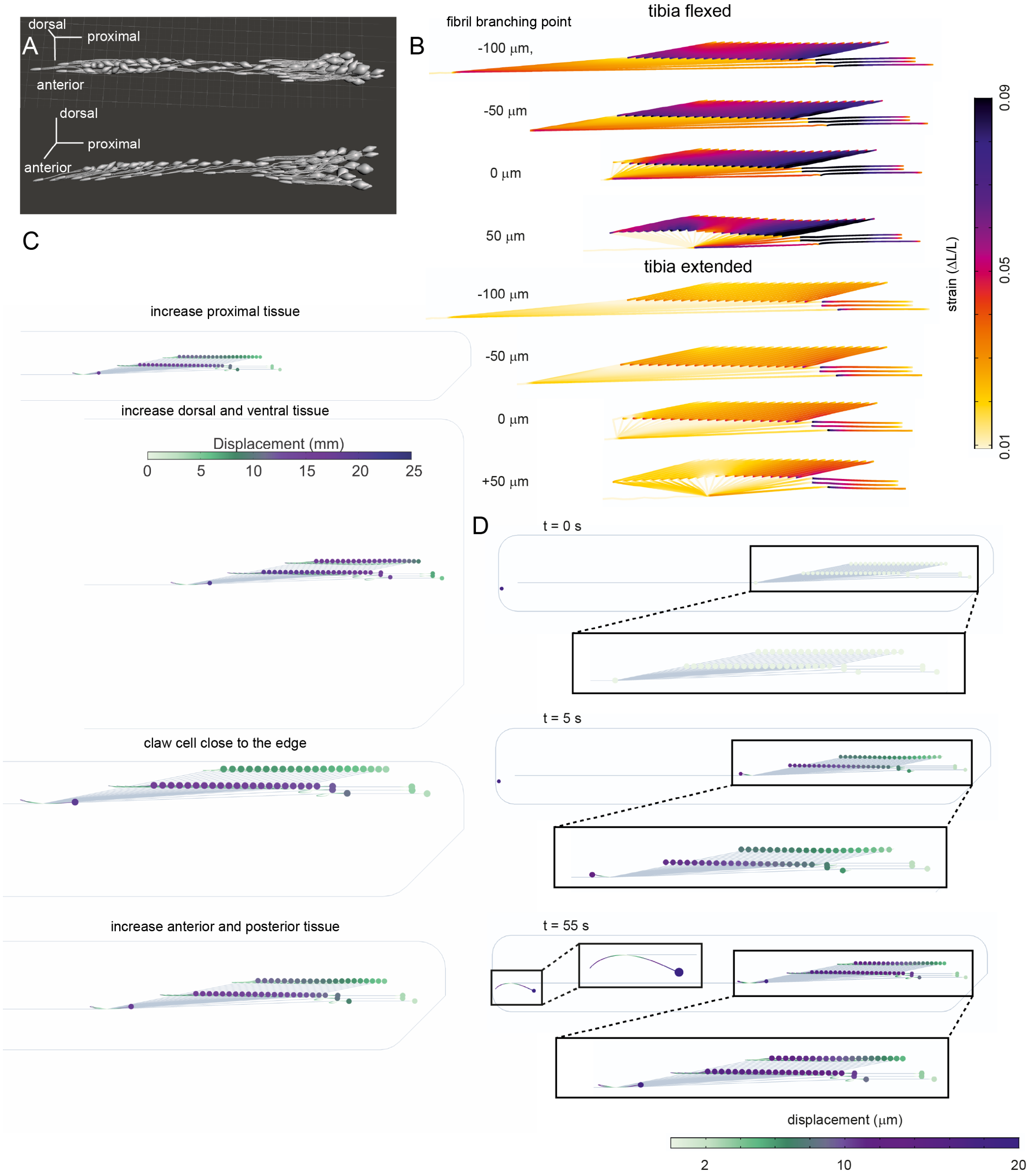

Figure S7. Details of the finite element model of claw neurons and tendon attachments. **(A)** A Blender model of claw and cap cells based on the X-ray reconstruction. **(B)** A map of strain in the dendrites of model claw cells during tibia flexion (top) and extension (bottom) when we moved the fibril branching point to different positions along the long axis of the femur. **(C)** Cell displacement maps showing how the properties of a tissue surrounding FeCO cells affect the movements of the claw cells and the cap cells during tibia flexion/extension. **(D)** Cell displacement maps showing the time course of the force application.

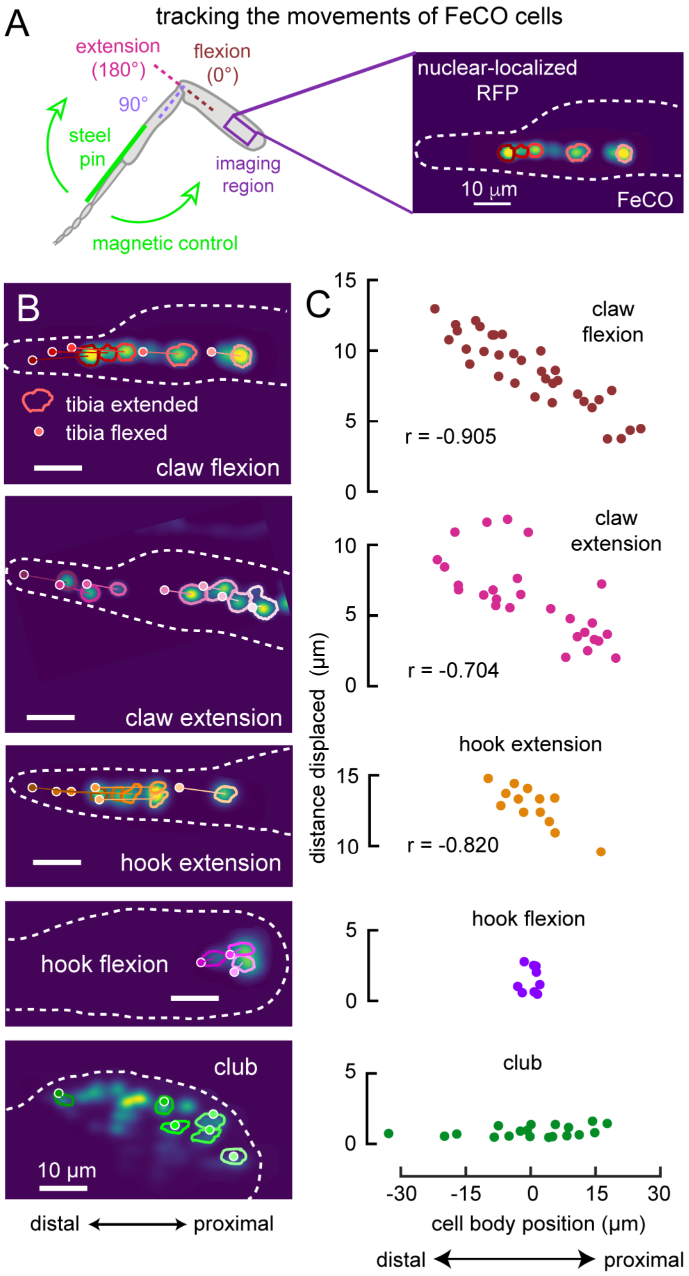

Fig. S8. Translation of FeCO cells during movement of the femur-tibia joint. **(A)** We tracked FeCO cell nuclei labeled with nuclear-localized RFP (each colored circle in the right image indicates the tracked cell nuclei) in the femur using transcuticular two-photon imaging, while swinging the tibia from extension to flexion with a magnetic control system. (**B**) Two-photon images of FeCO cell nuclei during full tibia extension. Tracked nuclei are outlined in the images. Lines connect the centroids of each nucleus during extension (proximal end of the line) and flexion (small circles with white edge). (**C**) Scatter plots showing the distance each cell moved between flexion and extension vs. the cell's position along the distal to proximal axis of the femur. We normalized the cell position within each fly by taking the centroid of all cells in that fly as zero and defining the distance to the proximal side as positive. (Number of flies: claw flexion = 4, claw extension = 7, hook extension = 3, hook flexion = 3, club = 3.)

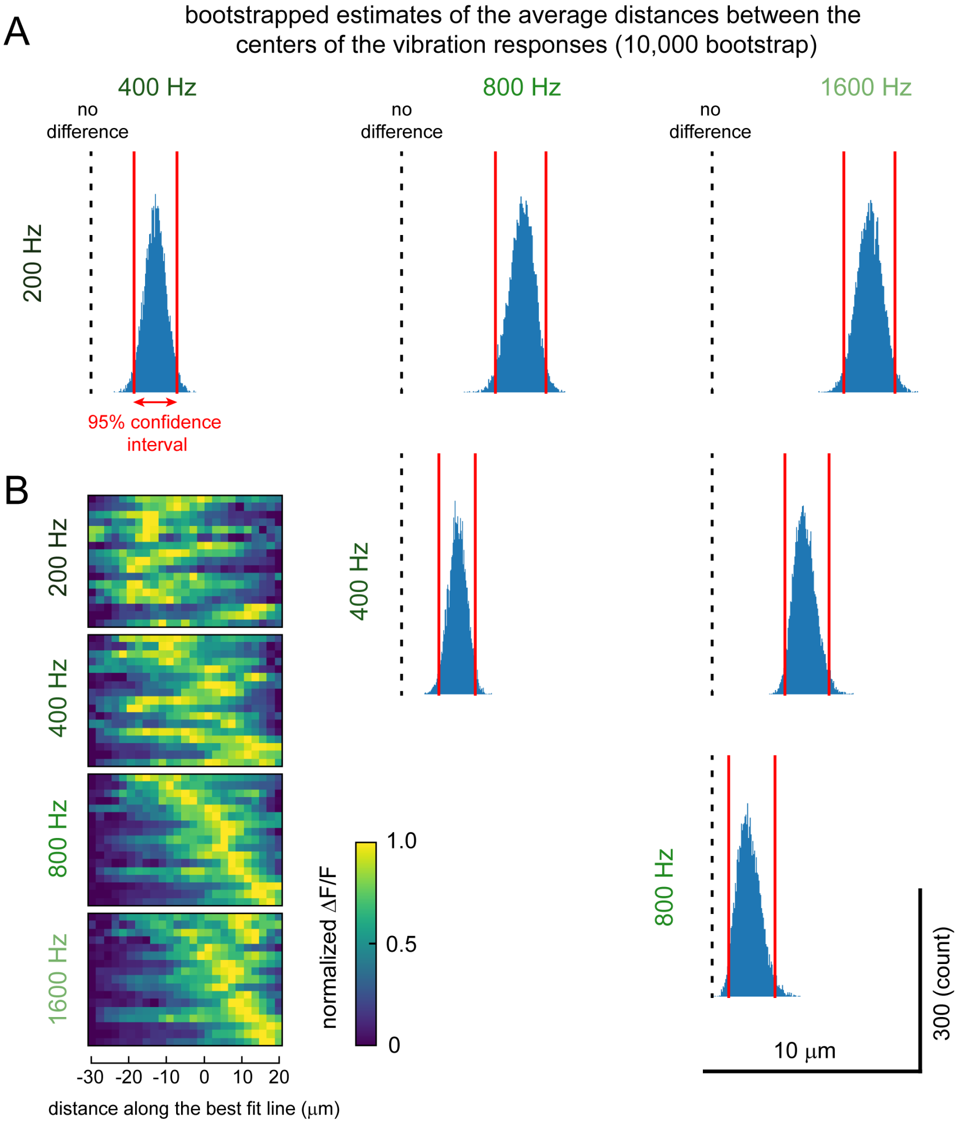

Figure S9. Further quantification of vibration responses in club dendrites (**Fig. 5**). Plots show bootstrapped estimates of the average distances between the centers of the responses to tibia vibrations at different frequencies and the distribution of the calcium activity along the best-fit line for the vibration response centers. **(A)** Histograms of the average distances between the centers of the responses to the tibia vibrations at different frequencies estimated with bootstrap analysis (n = 10,000 re-sampling from 17 flies). A pair of red vertical lines in each histogram show the 95% confidence interval of the average distances between the centers of the responses. Black dotted lines indicate no difference in the average location of the centers of the responses. Centers of the responses for tibia vibrations with different frequencies are all significantly different from each other. **(B)** Distribution of calcium activity (ΔF/F) along the line that best-fit the centers of the responses to tibia vibrations (a gray line in **Fig. 5D**) (n = 17 flies for each frequency). We normalized the calcium activity within each tibia vibration frequency for each fly to show the shift in the peak activity location.

Supplemental Movies

Movie S1. Organization of the femoral chordotonal organ, reconstructed from X-ray imaging of the *Drosophila* leg.

Movie S2. Reconstruction of femoral chordotonal organ (FeCO) sensory neurons and tendons from X-ray holographic nanotomography of the *Drosophila* leg.

Movie S3. Reconstruction of the arculum and femoral chordotonal organ (FeCO) tendons from X-ray holographic nanotomography (of the *Drosophila* leg.

Movie S4. Bright-field and two-photon imaging of arculum movements in the *Drosophila* leg.

Movie S5. Two-photon calcium imaging from femoral chordotonal organ (FeCO) cell bodies in the fly femur.

Movie S6. Two-photon calcium imaging from femoral chordotonal organ (FeCO) axons in the fly ventral nerve cord (VNC).

Movie S7. Changes in mechanical strain over time in a finite element model of claw neurons and tendon attachments.

Materials and Methods

Experimental animals

We used *Drosophila melanogaster* raised on standard cornmeal and molasses medium kept at 25 C in a 14:10 hour light:dark cycle. We used female flies 1 to 7 days post-eclosion for all imaging experiments, except for joint arculum imaging experiments where we occasionally used flies less than 1 day old to maximize transparency of the cuticle. The genotypes used for each experiment are listed in a table below.

Sample preparation for confocal imaging of brains and VNCs

For confocal imaging of VNCs, we crossed flies carrying the Gal4 driver to flies carrying pJFRC7-20XUAS-IVS-mCD8::GFP and dissected the VNC from female adults in PBS. We fixed the VNC in a 4% paraformaldehyde PBS solution for 20 min and then rinsed the VNC in PBS three times. We next put the VNC in blocking solution (5% normal goat serum in PBS with 0.2% Triton-X) for 20 min, then incubated it with a solution of primary antibody (chicken anti-GFP antibody 1:50; anti-brp mouse for nc82 neuropil staining; 1:50) in blocking solution for 24 hours at room temperature. At the end of the first incubation, we washed the VNC with PBS with 0.2% Triton-X (PBST) three times, then incubated the VNC in a solution of secondary antibody (anti-chicken-Alexa 488 1:250; anti-mouse-Alexa 633 1:250) dissolved in blocking solution for 24 hours at room temperature. Finally, we washed the VNC in PBST three times, once in PBS, and then mounted it on a slide with Vectashield (Vector Laboratories). We acquired z-stacks of each VNC on a confocal microscope (Zeiss 510).

For confocal imaging of ChaT co-labeled legs, we crossed flies carrying the Gal4 driver to flies carrying UAS-RedStinger; LexAopnlsGFP/CyO; ChAT-LexA/TM6B. We selected non-balancer female adults, and dissected legs while flies were anesthetized with CO2. We immediately fixed the legs in 4% formaldehyde in PBS with 0.2% Triton-X for 20 min and rinsed them in PBS three times over 30 minutes. We mounted the legs in VectaShield and acquired z-stacks on a confocal microscope (Zeiss 510).

For *in silico* overlay of the expression patterns of Gal4 lines (**Fig. S1**), we used confocal stacks of each Gal4 line with neuropil counterstaining (from the Janelia FlyLight database (Jenett et al., 2012)) and used the neuropil staining to align the expression pattern in the VNC using the Computational Morphometry Toolkit (CMTK (Jefferis et al., 2007); http://nitrc.org/projects/cmtk) to a female VNC template (Bogovic et al., 2020).

Sample preparation for confocal imaging of muscles, cuticle, and FeCO

To visualize the foreleg muscles, tendons and exoskeleton along with the FeCO, we expressed mCD8::GFP under control of *iav*-Gal4. Flies were anesthetized on ice, briefly washed with 70% ethanol, rinsed in PBS, and pinned onto Sylgar-coated Petri dish with 1 cm pins (Minuten Pins, Fine Science Tools # 26002-15) with their foreleg tibia in either fully levated, depressed or in an in-between position, under 2% paraformaldehyde/PBS/0,1% triton X-100, and fixed in this solution overnight at 4°C. The legs were removed at the coxa and after washing in PBS containing 1% triton X-100 (PBS-T), the samples were embedded in 7% agarose and sectioned on Leica Vibratome (VT1000s) in the plane perpendicular to the femur-tibia joint at 0.15 mm. The slices were incubated in PBS with 1% triton X-100, 0.5% DMSO, escin (0.05 mg/ml, Sigma-Aldrich, E1378), 3% normal goat serum (need the manufacturer), Texas Red-X Phalloidin (1:50, Life Technologies #T7471), anti-GFP rabbit polyclonal antibodies (1:1000, Thermo Fisher, #A10262) and a chitin-binding dye Calcofluor

White (0.1 mg/ml, Sigma-Aldrich #F3543-1G) at room temperature with agitation for 24 h. After a series of washes in PBS-T the sections were incubated for 24 h in the above buffer containing secondary antibodies (1:1000, Alexa 488-cojugated goat anti-rabbit, Thermo Fisher #A32731). The sections were washed and mounted in Tris-buffered (50 mM, pH 8.0) 80% glycerol, 1% DMSO between two #1 coverslips.

Sample preparation and confocal imaging of arculum and tendons

The flies were fixed as described above. The forelegs were removed by cutting at the trochanter-femur joint and the tibia was cut in half to create openings aiding penetration of the proteases. The soft tissues were digested away with a mixture of 0.25 mg/ml collagenase/dispase (Roche #10269638001) and 0.25 mg/ml hyaluronidase (Sigma Aldrich #H3884-100MG) in PBS-T overnight at 37°C. The cuticle's pigmentation was bleached with 20% peroxide for 4-5 hours and the exoskeleton and tendons were stained with Congo Red (0.5 mg/mL, Sigma-Aldrich #C676-25G) overnight. The samples were dehydrated in ethanol and mounted in methyl salicylate (Sigma-Aldrich #M6752).

Serial optical sections were obtained at 1 µm intervals on a Zeiss 880 confocal microscope with a LD-LCI 25x/0.8 NA objective, or at 0.5 µm with a Plan-Apochromat 40x/0.8 NA objective. Calcofluor White, anti-GFP/anti-rabbit Alexa 488 antibodies and Texas Red phalloidin-treated samples were imaged using 405, 488 and 594 nm lasers, respectively. The 560 nm laser line was used to excite Congo Red. Images were processed in Fiji (http://fiji.sc/), Icy (http://icy.bioimageanalysis.org/) and Photoshop (Adobe Systems Inc.). Fiji was used to generate .obj files (meshes) that were further processed and segmented in Blender (http://blender.org).

Segmentation of X-ray microscopy data

We used a previously published X-ray holographic nanotomography dataset of an adult fly's front leg (Kuan et al., 2020). From this dataset, we manually reconstructed FeCO structures using CATMAID (Saalfeld et al., 2009; Schneider-Mizell et al., 2016); the reconstruction can be accessed at https://radagast.hms.harvard.edu/catmaidvnc/61/links/Mamiya2022. Annotated structures, including FeCO cell bodies and cap cells, tendons, and the arculum, were then exported to Blender with the CATMAID-to-Blender plugin (Schlegel et al., 2016). Unlike a previous study (Shanbhag et al., 1992), we did not observe any connections between FeCO sensory structures and surrounding muscles in the femur.

Blender model of FeCO

We combined X-ray microscopy data mentioned above and confocal images of the foreleg exoskeleton to generate a blender model of FeCO. For modeling the arculum, we extracted the 3D model/mesh of the arculum from the confocal stack of the foreleg exoskeleton imaged with a 40x, NA 1.3 objective using Fiji's 3D viewer plugin (http://fiji.sc/). After importing the CATMAID files for the X-ray microscopy data into Blender (Community, B.O., 2018. Blender - a 3D modelling and rendering package, Stichting Blender Foundation, Amsterdam: http://www.blender.org) as described above, we fitted the arculum mesh manually to replace the original wireframe. For the neuronal cell bodies and cap cells, we slightly modified the CATMAID primitives (spheres and cylinders) to resemble the morphology of these cells in confocal microscopy images.

Fly preparation for *in vivo* two- or three-photon imaging of FeCO axons, FeCO cell bodies, and arculum in the VNC and leg

For recording the calcium activity of FeCO axons in the VNC while controlling tibia position, we used a fly holder and preparation procedures previously described by (Mamiya et al., 2018). First, we anesthetized the fly by briefly cooling them in a plastic tube on ice, then glued the fly onto a hole in a thin, translucent plastic sheet using UV-cured glue (Bondic). We put the fly's head through the hole, gluing it on the upper side of the fly holder. We glued the ventral side of the thorax to the hole. Abdomen and legs were placed on the bottom side of the holder. To control the femur-tibia joint angle, we glued down the femur of the right prothoracic leg to the holder and glued a small piece of insect pin (length ~1.0 mm, 0.1 mm diameter; Living Systems Instrumentation) to the tibia and the tarsus. We glued down all other legs away from the right prothoracic leg and bent the abdomen to the left side and glued it at that position to not interfere with the movement of the tibia of the right prothoracic leg. To enhance the contrast and improve the tracking of the tibia, we painted the pin with black India Ink (Super Black, Speedball Art Products). After immersing the top side of the preparation in *Drosophila* saline (containing 103 mM NaCl, 3 mM KCl, 5 mM TES, 8 mM trehalose, 10 mM glucose, 26 mM NaHCO3, 1 mM NaH2PO4, 1.5 mM CaCl2, and 4 mM MgCl2; pH 7.1; osmolality adjusted to 270-275 mOsm), we removed the cuticle on the ventral side of the prothoracic segment of the VNC with fine forceps. We removed the digestive tract to reduce the movements of the VNC and removed fat bodies and larger trachea to improve the optical access. We performed all recordings at room temperature.

For tracking the movements of arculum and FeCO cell nuclei or recording the calcium activity of FeCO cell bodies in the leg, we used a fly holder similar to the one described above, except that it either had a glass cover slip instead of plastic at the position where the right prothoracic femur was glued, or it was made of a thin metal sheet instead of plastic and there was a femur sized slit in the holder where the femur of the right prothoracic leg was placed. These changes allowed us to image the arculum and FeCO cell nuclei or cell bodies from above, through the cuticle, while controlling the tibia position from below the holder. For these experiments, we painted the pin with white paint to enhance its contrast against the glass cover slip or dark metal sheet. For leg imaging, we placed water between the fly holder and the objective and did not remove cuticle to avoid damaging the leg and FeCO.

In vivo image acquisition two- or three-photon imaging.

For imaging calcium activity from the axons of FeCO neurons and for tracking FeCO cell nuclei movements, we used a modified version of a custom two-photon microscope previously described in detail (Euler et al., 2009). We used a mode-locked Ti/Sapphire laser (Mira 900-F, Coherent) set at 930 nm for the excitation source and adjusted the laser power using a set of neutral density filters to keep the power at the back aperture of the objective (40x, 0.8 NA, 2.0 mm wd; Nikon Instruments) below ~25 mW during the experiment. For calcium imaging from the FeCO cell bodies in the leg and for simultaneous imaging of the cap cells and the claw cell nuclei, we used a Movable Objective Microscope (MOM; Sutter) with a mode-locked Ti/Sapphire laser (Coherent Vision) set at 920 nm for the excitation source and adjusted the laser power using a Pockels cell to keep the power at the back aperture of the objective (40x, 0.8 NA, 3.5 mm wd; Nikon Instruments) below ~25 mW during the experiment. For autofluorescence imaging of the arculum in the leg, we either used the two-photon Movable Objective Microscope mentioned above, or the three-photon excitation microscope. For three-photon excitation microscope, we generated excitation laser pulses with a commercial non-collinear OPA (Pera-F, Coherent) operating at 1300 nm pumped by a 40W fiber laser (Monaco, Coherent) operating at 1040 nm. We controlled the laser scanning mirrors and image acquisition of all microscopes with ScanImage software (version 5.7) (Pologruto et al., 2003) running in MATLAB (MathWorks).

To detect GCaMP7f fluorescence and the autofluorescence from the arculum, we used an ET510/80M (Chroma Technology Corporation) emission filter (VNC imaging) or a FF03-525/50-30 (Semrock) emission filter (cell body imaging / arculum imaging). For detecting RFP or tdTomato fluorescence, we used a 630 AF50/25R (Omega optical) emission filter (VNC and cell nuclei imaging) or a FF02-641/75-30 (Semrock) emission filter (cell body imaging). We amplified the fluorescence signals with GaAsP photomultiplier tubes (H7422P-40 modified version without cooling for VNC and cell nuclei imaging; H10770PA-40 for leg imaging and the arculum imaging; Hamamatsu Photonics).

For VNC axon recordings and cell nuclei tracking, we acquired images (256 x 120 pixels) at 8.01 Hz from the axon terminals of major axon bundles of FeCO neurons, or from the proximal region of femur where FeCO cell nuclei are located. For recordings of FeCO cell bodies, dendrites, or the arculum, we acquired fast z stacks of images (for cell bodies, 512 x 250~300 pixels, 4~7 z-levels; for dendrites, 512 x 512 pixels, 6 z-levels; for the arculum, 512 x 256 pixels, 7 z-levels) using resonant scanner and piezo controlled objective (acquisition rate for cell bodies, 9.6~16.8 Hz; for dendrites, 5 Hz; for the arculum, 8.51 Hz). We adjusted the image size and stack depth to capture most of the cell bodies, dendrites, or the arculum throughout each trial. At the end of the experiment, we acquired a z stack of the imaged regions to confirm the recording location.

Controlling tibia position using a magnet-motor system

We used a magnetic control system previously described in detail (Mamiya et al 2018) to control the femur-tibia angle during both the recordings from the axon terminals in the VNC and the cell bodies in the leg. We moved the tibia/pin to different positions by magnetically pulling them using a rare earth magnet (1 cm height x 5 mm diameter column). To precisely control the speed and position, we attached the magnet to a steel post (M3 x 20 mm flat head machine screw) and controlled its position using a programmable servo motor (SilverMax QCI-X23C-1; Max speed 24,000 deg/s, Position resolution 0.045 deg; QuickSilver Controls). To vibrate the tibia at high frequency, we placed a piezoelectric crystal (PA3JEW; ThorLabs) between the magnet and the steel post. We placed the motor on a micromanipulator (MP-285, Sutter Instruments) and adjusted its position so that the magnet moved in a circular trajectory centered at the femur-tibia joint, with the top edge of the magnet at approximately the same height as the tibia/pin. The inner edge of the magnet was ~1.5 mm from the center of the femur-tibia joint and the distance between the pin and the magnet was ~ 300 µm. We controlled the speed and the position of the servo motor with a custom script written in QuickControl software (QuickSilver Controls). For each trial, we confirmed the movement and the position of the tibia-femur joint using a high-speed video camera and machine vision algorithms described below.

Because it is difficult to fully flex the femur-tibia joint without the magnet colliding with the abdomen or other legs, we only flexed the joint up to ~ 18°. For swing motion trials, we commanded the motor to move between fully extended position (180°) and fully flexed position (18°) in one continuous sweep at a set speed of 360 deg/s (axon terminal imaging) or 5 deg/s (cell body imaging). For faster swing trials, we had a 5 s interval between the flexion and the extension movements, and we repeated the swing motion 6 times with a 5 s inter-trial interval. For slower swing trials, we had a 2 s interval between the flexion and the extension movements, and we repeated the swing motion 3 times with a ~30 s inter-trial interval. Because responses to each repetition of the swing motion were similar, we averaged the responses to the swing motion across the trials.

For ramp-and-hold motion trials (axon terminal imaging), we commanded the motor to move in 18° steps between the fully extended position and fully flexed position at 240 deg/s. Between each ramp movements, the leg was held at the same position for 3 s. We repeated each type of ramp-and-hold motion 3 times and averaged the responses across trials within each fly.

For both types of movements, we set the acceleration of the motor to 72000 deg/s^2. Movements of the tibia varied slightly across trials and flies due to several factors, including a small offset between the center of the motor rotation and the femur-tibia joint, resistance to the magnetic force by the fly, interference by physical contact between the tibia/pin and the holder or abdomen/legs. Because these variations were relatively small, we did not consider these differences in the summary of the responses (**Fig. 1D**, **S3F**). However, when quantifying the relationship between the femur-tibia angle and the cell activity (**Fig. 4C**) or movement (**Fig. 3C, S5, S6**), we plotted the response against the actual femur-tibia angle during each trial.

Tracking the femur-tibia joint angle

To track the position of the tibia/pin during the trials, we recorded videos (200 fps) using an IR sensitive high speed video camera (Basler Ace A800-510um, Basler AG) with a 1.0x InfiniStix lens (94 mm wd, Infinity). For VNC recording experiments, we used an 850 nm IR LED (M850F2, ThorLabs) to backlight the black painted tibia/pin through the translucent plastic fly holder. For leg recording experiments that required the metal fly holder, we front-lit the white painted tibia/pin using the same LED. In both cases, we used a 900 nm short pass filter (Edmund Optics) to filter out the two-photon excitation laser light. Because the servo motor was placed directly under the fly, we placed the camera to the side and used a prism (Edmund Optics) to capture the view from below. To synchronize the camera's images with two-photon microscope's laser scanned images, we acquired both the camera's exposure signal and the galvo scanner's Y axis scanning signal at 20 kHz.

For tracking the black painted tibia/pin position in the backlighted image (VNC recordings), we first selected the pixels below the threshold to detect the tibia/pin. We then approximated the orientation of the tibia/pin as the long axis of an ellipse fitted to these pixels (Haralick and Shapiro, 1992). In the front-lit setup (cell body recordings), lighting varied significantly throughout the trial due to shadows cast by the fly's body and the magnet. Because of this, we used DeepLabCut (Mathis et al., 2018) to track the tibia/pin. We trained the neural network to track 5 points along the femur and tibia/pin and approximated the orientation of each body part by fitting a line through the tracked 5 points using principal component analysis. The spatial resolution of the camera image was 3.85 µm per pixel and, assuming circular movement of the tibia/pin, 1-pixel movement at the edge of the tibia/pin (~1.2 mm from the center of the rotation) corresponded to 0.18°.

Vibrating the tibia using a piezoelectric crystal

To test the responses of the axons and dendrites of FeCO neurons to high frequency vibrations of the tibia, we attached the magnet to the tibia/pin and moved it using a piezoelectric crystal (PA3JEW, Max displacement 1.8 µm; ThorLabs). For controlling the movement of the piezoelectric crystal, we generated command waveforms in MATLAB and sent them to the piezo through a single channel open-loop piezo controller (Thorlabs). Because previous calibration of this piezoelectric crystal's movement in response to sine waves of different frequencies (Mamiya et al., 2018) showed that the power of oscillation at the target frequency drops greatly when the frequency of the command sine wave exceeds 2000 Hz, we used vibration in the range of 100 – 1600 Hz (sampling frequency 10 kHz). For each frequency, we presented 4 s of vibration twice with an inter-stimulus interval of 8 s.

Processing and analysis of *in vivo* imaging data

We performed image processing and analyses using scripts written in MATLAB (MathWorks) and Python. For all recordings, we first applied a Gaussian filter (kernel size 5x5 pixel, $\sigma = 3$) to the acquired images to reduce noise. For the recordings of FeCO axon terminals in the VNC, we aligned the filtered images (registered to ¼ pixel) to a mean image of the trial using a sub-pixel image registration algorithm (Guizar-Sicairos et al., 2008). For this alignment, we used the tdTomato fluorescence, which does not change as a function of intracellular calcium concentration. tdTomato fluorescence was stable over the course of the experiment, indicating that movement artifacts were absent or small for the VNC recordings. Thus, for these experiments we used the change in GCaMP7f fluorescence relative to the baseline ($\Delta F/F$) as the indicator of the calcium activity. To calculate $\Delta F/F$, we first selected pixels whose mean GCaMP7f fluorescence was above a set threshold (150 arbitrary units) and used the lowest average fluorescence level of these pixels in a 10-frame window as the baseline fluorescence during the trial. Because split-Gal4 lines drove GCaMP7f in one functional type of FeCO neurons, we averaged the responses of all pixels for these experiments. For claw-extension split-Gal4 line that drove expression in primarily extension-tuned claw neurons, but also occasionally labeled flexion-tuned neurons, we first separated the selected pixels into two groups based on the similarity of their intensity change during the trial using k-means clustering of pixel correlations (Mamiya et al., 2018). We then calculated the average Δ F/F for each group of pixels. When analyzing vibration responses in the axons, we took an average activity level in a 1.25 s window starting 1.25 s after the vibration onset as a measure of response amplitude. We further averaged the responses within each fly before averaging across flies.

For recordings of FeCO cell nuclei and cell bodies in the leg, we found that different cell bodies move by different amounts during the flexion/extension of the joint. Thus, we did not attempt to align these images to the mean image for these recordings. Rather, we used a cell tracking algorithm described below, or manual labeling of each cell nuclei in the image to track the position of each cell during the trial. Most of the cell movements occurred in the x-y direction of the imaging plane. Thus, for recordings with fast z-stacks (cell body imaging), we first averaged the images acquired from the different z-levels for each time point to be able to track cell bodies at the different z-levels simultaneously. Then we selected pixels whose mean RFP (cell nuclei tracking) or tdTomato (cell body imaging) fluorescence was above a set threshold (20 – 150 arbitrary unit), resulting in groups of pixels shaped similar to the cell nuclei or cell bodies with higher intensity fluorescence in the middle of the cell. We used this fluorescence intensity pattern to perform a watershed segmentation of each image to identify cell nuclei or cell bodies. We also used the same algorithm to identify the autofluorescence from the arculum in each image and track it during tibia flexion/extension. Because simple watershed segmentation often leads to over-segmentation of the image, we first chose a key frame in the trial, and manually merged the over-segmented sections so that the segmentations matched the cells in this image. Then, we used the centroids of these segmented cells as the seeds to perform watershed segmentation of the image corresponding to the next frame. Because the cell movements between each imaging frame were small compared to the cell size (for slow swing trials), this procedure allowed us to track the movements of the cell by updating the centroid of each cell as it moved. We repeated this process until we labeled all frames in this manner. To reduce noise in the labeling process, we selected three key frames per trial (located at the beginning, middle, and the end of the trial) to generate three different sets of labels for each frame. Then we merged these labels together by taking pixels whose label identity agreed in at least two of the three labels. Watershed segmentation relies on the intensity pattern of the fluorescence for segmentation, and because some lines label cells that are in close proximity, it was difficult to segment out these overlapping cells. In these cases, we chose to group these cells together. Thus, our segmentation is a conservative estimate of the cells in the recordings, and may sometimes contain segments that are composed of multiple cells. Because tdTomato fluorescence fluctuated as the cell moved inside the leg (presumably due to different parts of cuticle and leg transmitting different amounts of light), we used the changes in the ratio between the GCaMP fluorescence and tdTomato fluorescence relative to the baseline ratio ($\Delta R/R$) from each cell as the indicator of the calcium activity. For each cell, we used the lowest average ratio in a 12-frame window as the baseline ratio during the trial. For cells labeled with the claw-extension split-Gal4 line that occasionally drove expression in flexion-tuned neurons and those labeled with the claw-Gal4 line (GMR73D10), we categorized the cells into flexion-tuned or extension-tuned based on their peak responses to tibia angle.

Analyzing the relationship between the position and activity of claw neuron cell bodies

To investigate the relationship between the position of claw neurons and their activity patterns, we measured each segmented claw neuron's position along the long axis of the femur. Cell bodies of the claw neurons are aligned in a blade-like array along the long axis of the femur and we approximated this axis by fitting a line through the centroid of the segmented cells using principal component analysis. We used the position of each segmented cell body's centroid along this axis when the tibia angle was 90˚ (average of the cell's position when 87.5˚ <= tibia angle <= 90˚) as a measure of the cell's equilibrium position. Because claw neurons' maximum response amplitudes varied from neuron to neuron, we looked at the relationship between the tibia angle when the claw neuron's activity has reached 50% of the maximum activity (**Fig. 4B-C, S6**).

Quantifying the map of vibration frequency in the dendrites of club neurons

Within the FeCO, the dendrites of the club neurons responded most strongly and consistently to tibia vibration. Thus, we focused our analysis to the club dendrites and manually identified the region that corresponds to the dendrites of the club neurons (ROI) at each z-level for each fly (6 z-levels). To quantify the spatial pattern of activity, we first measured the changes in GCaMP7f fluorescence during the tibia vibration relative to the baseline ($\Delta F/F$) for each ROI at each z-level. Because most of the changes in the activity pattern was in x-y direction, we next took an average $\Delta F/F$ value along the z-axis to generate a 2D map of the activity pattern and calculated the weighted center of the activity. To compare the activity pattern between flies, we re-oriented the $\Delta F/F$ map so that the club dendrites were horizontal in all the maps. We also normalized the location of the center of the activity by using the center point of the dendritic tips of club neurons as the origin. To determine the center point of the dendritic tips, we looked at the most distal layer of dendritic tips and took the midpoint between the most dorsal and ventral dendritic tips.

For bootstrapped estimates of the average distances between the centers of the vibration responses, we first calculated the distances between the response centers for different pairs of vibration frequencies (from 200 to 1600 Hz) in each fly ($n = 17$ flies). Then, for each pair of vibration frequencies, we resampled the distances with replacement and calculated the average distance between the response centers 10,000 times. We looked at the 95% confidence intervals of the average distances between the response centers and checked whether the confidence intervals overlapped with zero distance (no difference between the locations of the response centers).

For calculating the response distribution along the best-fit line, we binned the pixels based on the distance along this line (2 μm/bin) and averaged their ΔF/F values. For each vibration frequency in each fly, we normalized the response distribution by its maximum response (n = 17 flies). In each distribution map, we ordered the flies based on the maximum response location during the 800 Hz tibia vibration.

For calculating the frequency response turning curve, we used pixels in the ROI that had the baseline fluorescence level above the background (background fluorescence level in each prep was identified by plotting the histogram of pixel intensities and finding a threshold that best distinguish background pixels from those that have GCaMP7f expression. Typically, there are two distributions of the pixel intensity, one that corresponds to the background pixels (narrow distribution at the low pixel intensity) and wider distribution of brighter pixels that corresponds to GCaMP7f expression). We calculated the average change in GCaMP7f fluorescence relative to the baseline for these pixels and used it as a measure of the activity (average for two stimuli in each fly for each frequency).

Finite Element Model of the arculum

We developed a finite element model (FEM) to study how the arculum moved in response to the forces applied to it *via* the femur-tibia joint. FEM was carried out using COMSOL Multiphysics (ver.5.5, Massachusetts, USA). Models were developed in the structural mechanics module and all components were modeled as simple linear elastic materials with linear behavior that follows Hooke's law.

We based arculum geometry on the 3D Blender model of the arculum and tendons reconstructed from confocal images and X-ray microscopy data (**Fig. 2**). This mesh was then imported into Meshmixer. After removing the joint and tendon attachments, we generated an STL file and imported the model into COMSOL. The 3D model was meshed using tetrahedral elements with triangular surface faces. We used the extremely fine setting of the physics controlled meshing. This uses a minimum element of 0.63 um and allows a maximum element size of 3.5 um. The model uses smaller elements in narrow regions of the arculum, specifically where the medial and lateral tendons attached to it in order to more carefully calculate strains and stresses as they develop in these regions. The complete geometry was represented by >35k elements.

Arculum material properties

We modeled the arculum as a linear elastic material. Most insect cuticle lies within a narrow range of densities of ~1200 kg/m^3 (Vincent and Wegst, 2004) and the arculum was modelled with this density. We used Poisson's ratio of 0.3, which is common for most materials in nature. The exact Young's modulus of the arculum is not known. Video and UV fluorescence data suggests that it contains some resilin but is stiffer than the resilin containing tendons that anchor it within the femur. There are different estimates for the Young's modulus for resilin and here we use 1.8 MPa (Frantsevich et al., 2019; Gosline et al., 2002). For our main model, we use a Young's modulus of 3.6 MPa (twice that of resilin) for the arculum, and we also performed a parameter sensitivity study for this input parameter. In the femur, the arculum is suspended within femoral tissue and is expected to encounter a high level of damping due to friction. Thus, to mimic these conditions, we applied a high isotropic damping factor of 0.5 to the arculum.

Arculum boundary conditions

The arculum is suspended in place in the femur by 4 tendon attachments. These are the joint tendon from the tibia-femoral joint, the extensor tendon to the extensor muscle within the femur, and the medial and lateral tendons to the FeCO. We treated each of these attachments as the boundary conditions experienced by the arculum. Each attachment is modelled as a spring and the attachment points are demarcated on the arculum model. The joint, medial, and lateral tendons are modelled as running parallel to the long axis of the femur (x axis) and the extensor tendon is modelled as making a 45° angle between the x and z axes. We treated each tendon as a stiff element whose spring constant is calculated using the following formula,

$$k = \frac{E_{res}A}{L_0}$$

Where, E_{res} is the Young's modulus of resilin, L_0 is the equilibrium length of the tendon, and "*A*" is the cross sectional area of the tendon. Based on the X-ray microscopy data, we used the following values to model each tendon:

Tendon name	**Equilibrium length (um)**	**Cross sectional area (um^2)**
Joint tendon	72	295.3
Femoral tendon	225	295.3
Medial tendon	268	50.9
Lateral tendon	283	57.2

We observed that the proximal edge of the medial tendon attached to the FeCO undergoes large translation movements during joint flexion (**Fig. 3**, **S8**). This suggests that this tendon is effectively coupled to a soft spring on the proximal side. To model this, we treated this tendon as having a spring constant lowered by a factor of 2. We also performed a parameter sensitivity analysis to test the effect of this approximation. Finally, the spring foundations were initialized as being in equilibrium, i.e. not applying any forces on the arculum unless moved from initial positions. Each spring foundation was also modelled as experiencing significant damping along its axis (isotropic loss factor =0.5).

Loads generated during joint rotation

During joint flexion, loads are applied to the arculum and these loads are in turn transmitted to the FeCO via the medial and lateral tendons. Bright-field imaging (**Movie S4**) showed that the joint tendon converts the rotation experienced by the tibia into a linear movement. This suggests that the joint tendon converts joint torque into a linear force along the long axis of the femur (x axis). We modelled this force as a periodic 10 uN force applied at the attachment area of the joint tendon parallel to the x axis. This approximates force levels known to be produced by *Drosophila* muscles (Azevedo et al., 2020). Since the model follows linear Hookean mechanics, an increased force should simply lead to a linear increase in the movements of the arculum, as long as the forces are below the point where the force cause plastic deformation or buckling of the arculum. We tested the behavior of the model for a period force from 2 Hz to 80 kHz, where the 2nd eigenfrequency of the system was observed. We used a frequency domain study, simulating either 20 or 5 frequency steps per frequency decade depending on the study.

Models to investigate joint angle selectivity in claw cells

We used a series of finite element models to study the selectivity of claw cells to different femur-tibia joint angles. We found that the claw cells, the medial tendon, and the fibrils emanating from the medial tendon and attaching to the claw cell dendrites were all symmetric around a single plane through the leg (**Fig. S7A**). Thus, we assumed that a simplified two-dimensional model could capture the mechanics of the system without significant loss of fidelity (**Fig. 3D**).

We developed these two-dimensional models using the truss and solid mechanics interfaces within structural mechanics module in COMSOL Multiphysics (ver.5.5, Massachusetts, USA). We modelled the medial tendon, the fibrils, and the claw cell dendrites as truss elements, i.e. as slender ‘string’-like structures with low to negligible bending stiffness. We modelled the tissue surrounding these elements as a solid with a defined and uniform thickness. The two physics interfaces were coupled by having them solve for the same dependent displacement variables. All components were modeled as simple linear elastic materials with linear behavior that follows Hooke’s law.

System geometry

We simplified the reconstructed 3D geometry of the FeCO into a 2D geometry in COMSOL (**Fig. 3D**). The medial tendon was modelled as a 250 µm truss with a circular cross section with a radius of 2 µm. Each dendrite was modelled as a 50 um truss with a thinner circular cross section (radius of 0.2 µm). Both the tendon and fibrils were modelled as being constrained to remain straight, to capture their higher bending stiffness. 20 dendrites were modelled as laying parallel to each other and at an angle of 168° to the long axis of the medial tendon. 3 dendrites were also modelled as lying in parallel to the medial tendon to represent the claw cells at the most proximal end of the FeCO. Overall, we see relatively low bending in the truss elements, and their shape is stabilized by surrounding tissue.

In the real FeCO, there are two sets of claw cells and dendrites, attached to the same cap cell array. Each array of cells lies in a plane, and the two planes are at about 45 degrees to each other. The dissecting plane between these two cell arrays lies along the ventral dorsal axis of the femur. Thus, forces applied by the medial tendon along the dorsal ventral and proximal distal planes, would be symmetrically applied to both arrays of neurons. In order to reduce the computational problems, we decided to use the symmetry between the two neuronal arrays and simplify this geometry into a 2D system. Therefore, we represent both arrays of cells by a single planar array, which maintains all other geometric features of each array.

We used a single vertex at each end of dendrites to model the position of each cap and claw cell. We treated each cell as a point mass. The mass of each cell was set by assuming that the they are spheres with a density of 1200 kg/m^3 and radius of 4 µm for the claw cell and 2 µm for the cap cell. Fibrils were modelled by attaching the proximal tip of the medial tendon to each cap cell. In this geometry, it is the fibrils radiating from the tip of the medial tendon to the cap cells that form a radiating array with an angular gradient from 168° to 180°. It is this angular gradient of fibrils that gives rise to the strain gradient observed in the FeCO. Repositioning the branching point changes the strain gradient within the FeCO. A distal to proximal strain gradient was generated within the FeCO only while the branching point remained distal to the most distal cap cell (**Fig. S7B**).

Finally, we embedded this truss structure in a solid with a uniform thickness (z-axis) of 10 µm, length of 520 µm, and width of 80 µm. This structure very roughly approximates the shape of the extra-cellular matrix within the femur around the FeCO. The edges of the solid are chamfered to retain the rounded structure of the leg and to prevent accumulation of stresses in corners. The solid is also narrowed proximally near the FeCO, where the femur connects to the next leg segment. The truss is placed so that the cap and claw cells are roughly symmetrically embedded within the height of the tissue, and the entire medial tendon is within the tissue space.

By varying the geometry systematically, we found that the 2D section of this solid does not have strong effects on the behavior of interest, the displacements of the cap and claw cells and the strain gradient in the FeCO dendrite array. For instance, if the solid is significantly longer and extends well beyond the FeCO, or if its height is significantly greater, this does not significantly change the pattern of strain that develops within the dendrite array (**Fig. S7C**). One geometric feature that does have a small effect is proximity of the FeCO to the edges of the solid. The cells closest to the edge of the solid experience drag-like effects from the immobile wall, and undergo slightly less displacement than those that are further away, thereby altering the absolute strain level developed in the dendrites but not the gradient **(Fig. S7C).**

The model was meshed using 20 edge elements for each truss, i.e. for the medial tendon, each fibril and dendrite. The solid was meshed using triangular elements using the normal physics controlled meshing. This uses a minimum element of 0.15 µm and allows a maximum element size of 34.8 µm. The model uses smaller elements near the FeCO, and in the narrower corners of the solid, in order to more carefully calculate strains and stresses as they develop in these regions. The complete geometry was represented by 3495 triangle elements and 1081 edge elements.

System material properties

We treated all parts of the model as linear elastic materials. Most insect cuticle lies within a narrow range of densities of ~1200 kg/m^3 (Vincent and Wegst, 2004) and all parts were modelled with this density. Most materials in nature have a Poisson's ratio of 0.3, which was similarly uniformly applied. The exact Young's modulus of the medial tendon is not known. Like the arculum, UV fluorescence data suggests that it contains some resilin. Again, here we used 1.8 MPa as the Young's modulus for the medial tendon and the thinner fibrils arising from it (Frantsevich et al., 2019; Gosline et al., 2002). For the ciliated dendrites of the claw cells, we used 178 kPa, an estimate of ciliary Young's modulus made by previous authors (Rydholm et al., 2010).

We do not know the exact Young's modulus of the tissue surrounding the FeCO. However, Young's modulus of the soft biological tissues are known to range from ~100 Pa (mammalian brain) to several MPa (mammalian cartilage) (Levental et al., 2007). We expect the internal tissue of fly legs to be relatively soft. We tested the behavior of our model when the solid around the FeCO was set to a range of Young's moduli between 100 Pa and 2 kPa. We found that when the modulus was set to 1 kPa, it reasonably reproduced the motions of cap and claw cells observed experimentally (**Fig. 3F, S5A-B**). Thus, we used this value in all models. This supports the idea that the internal tissue in the fly leg is relatively soft.

However, we found that tissue stiffness interacts with the modelled thickness of the solid. If the solid's thickness is increased by an order of magnitude (to 100 µm), then the Young's modulus of the solid needs to be decreased by an order of magnitude (100 Pa) to recover the same level of cell displacement and strain gradient seen in the thinner stiffer solid (10 µm, 1 kPa). This is in contrast to the behavior near the immobile tissue wall. This is because in this 3rd dimension in the 2D model, there is no mechanism by which to set the wall as being immobile, and no drag like effects from the wall are observed. What we observe is that in conditions where the tissue edge is mobile, thinner tissue will allow greater motion, and thicker tissue resists motion. In the real tissue, the stiffness of the extra-cellular matrix is likely tuned by inclusion of different concentrations of structural protein (Levental et al., 2007). We expect that in the real system, the tissue's width, thickness, and stiffness are tuned for appropriate functioning.

A high level of material damping was applied both to the truss and solid material to account for the high viscous damping encountered by small structures immersed in fluid. For the sake of simplicity, we ignored any material anisotropy in this tissue. In the real system, given the orientation of the fibers within the matrix, and the neurons juxtaposing the claw cells, there is likely some anisotropy. However, since these properties are difficult to estimate, we begin with a simplified system where soft isotropic tissue surrounds the FeCO and found that it can still reproduce most of the mechanics of interest. Further tuning of the model might recover all measured features of the mechanics, but at the cost of further assumptions, accompanied by lower explanatory power.

Boundary conditions

We embedded and coupled the truss structure to the solid in the equilibrium position but otherwise left it unconstrained. We expect the tissue surrounding the FeCO to be bounded by other stiffer tissue along the edge and likely has a no-slip condition. Therefore, the solid that modelled the tissue surrounding the FeCO had fixed external boundaries, i.e. the solid could not move at the edges.

Application of the forces

To simulate the forces applied to the claw cells in the FeCO by the slow flexion and extension of the tibia, we measured the movement of center of mass of the arculum from flexion to extension from 12° to 176° at the rate of 3.28 °/s over 50s (**Fig. 2G**). We also measured the angle of the arculum over the same movement (**Fig. S4B**). From this, we can calculate the position of the attachment of the medial tendon to the arculum. Thus, we know the position of the distal end of the medial tendon as the leg joint is flexed/extended.

We used this positional information to apply a force to the modelled system. A prescribed displacement was applied at the distal point on the modelled medial tendon over the same period of time (**Fig. S7D**). Thus, the model was solved in the time domain and the displacement field of the whole geometry was calculated as it changed in time. Since in the real measurements, the arculum position was initiated at a flexed angle (12°), and not at the equilibrium 90° angle, we needed to use the same paradigm in the model. The model was initiated at the flexed position, i.e. the distal end of the medial tendon was drawn back from the equilibrium position (90°) to the position it would occupy when the joint was flexed to 12°. The model was allowed to equilibrate into this position, since moving the FeCO from its equilibrium position will generate a large transient strain in the system, which is not relevant to our question. No movement was applied to the medial tendon for 5 seconds. Only after, the transient strain had decayed and the full steady state strain had formed, was the medial tendon in the model displaced. It was displaced with the same dynamics as were observed in the real data, thus replicating the observed forcing regime in the model. In all subsequent analysis, we consider model behavior only after the initial 5 seconds.

Table of genotypes

Fig. 1A, F – iav-Gal4 driving GFP expression	w[1118]; pJFRC7-020XUAS-IVS-mCD8::GFP (attp40); P{w[+mC]=iav-GAL4.K}3
Fig. 1C – all FeCO cells	w[1118]; P{w[+m*]=lexAop-2xhrGFP.nls}2b; Mi{Trojan-LexA:QFAD.0}ChAT[MI04508-TLexA:QFAD.0]
Fig. 1C – hook flexion	P{w[+mC]=UAS-RedStinger}3, w[1118] / w[1118]; P{y[+t7.7] w[+mC]= VT038873-p65ADZ}attP40 / +; P{y[+t7.7] w[+mC]=R32H08-GAL4.DBD}attP2 / +
Fig. 1C – hook extension	P{w[+mC]=UAS-RedStinger}3, w[1118] / w[1118]; P{y[+t7.7] w[+mC]= VT018774-p65ADZ}attP40 / +; P{y[+t7.7] w[+mC]=VT040547-GAL4.DBD}attP2 / +
Fig. 1C – claw flexion	P{w[+mC]=UAS-RedStinger}3, w[1118] / w[1118]; P{y[+t7.7] w[+mC]=R92D04-p65.AD}attP40 / +; P{y[+t7.7] w[+mC]=VT043140-GAL4.DBD}attP2 / +
Fig. 1C – claw extension	P{w[+mC]=UAS-RedStinger}3, w[1118] / w[1118]; P{y[+t7.7] w[+mC]=R55C05-p65.AD}attP40 / +; P{y[+t7.7] w[+mC]=VT017745-GAL4.DBD}attP2 / +
Fig. 1C – club	P{w[+mC]=UAS-RedStinger}3, w[1118] / w[1118]; P{y[+t7.7] w[+mC]= 50C12-p65ADZp}JK22C / +; P{y[+t7.7] w[+mC]=R84H05-GAL4.DBD}attP2 / +
Fig. 1D – hook flexion	w[1118]; P{y[+t7.7] w[+mC]= VT038873-p65ADZ}attP40 / P{w[+mC]=UAS-tdTom.S}2; P{y[+t7.7] w[+mC]=R32H08-GAL4.DBD}attP2 / P{y[+t7.7] w[+mC]=20XUAS-IVS-jGCaMP7f}VK00005
Fig. 1D – hook extension	w[1118]; P{y[+t7.7] w[+mC]= VT018774-p65ADZ}attP40 / P{w[+mC]=UAS-tdTom.S}2; P{y[+t7.7] w[+mC]=VT040547-GAL4.DBD}attP2 / P{y[+t7.7] w[+mC]=20XUAS-IVS-jGCaMP7f}VK00005
Fig. 1D – claw flexion	w[1118]; P{y[+t7.7] w[+mC]=R92D04-p65.AD}attP40 / P{w[+mC]=UAS-tdTom.S}2; P{y[+t7.7] w[+mC]=VT043140-GAL4.DBD}attP2 / P{y[+t7.7] w[+mC]=20XUAS-IVS-jGCaMP7f}VK00005
Fig. 1D – claw extension	w[1118]; P{y[+t7.7] w[+mC]=R55C05-p65.AD}attP40 / P{w[+mC]=UAS-tdTom.S}2; P{y[+t7.7] w[+mC]=VT017745-GAL4.DBD}attP2 / P{y[+t7.7] w[+mC]=20XUAS-IVS-jGCaMP7f}VK00005

Fig. 1D – club	w[1118]; P{y[+t7.7] w[+mC]= 50C12-p65ADZp}JK22C / P{w[+mC]=UAS-tdTom.S}2; P{y[+t7.7] w[+mC]=R84H05-GAL4.DBD}attP2 / P{y[+t7.7] w[+mC]=20XUAS-IVS-jGCaMP7f}VK00005
Fig. 3A-C, E – claw cell and cap cells labeled with RFP and GFP	w[1118]; P{w[+mC]=nompA.GFP}5-3 / P{w[+mC]=UAS-RedStinger}4; P{y[+t7.7] w[+mC]=GMR73D10-GAL4}attP2
Fig. 4A-C, E-F – claw flexion neurons expressing tdTomato and GCaMP7f	w[1118]; P{y[+t7.7] w[+mC]=R92D04-p65.AD}attP40 / P{w[+mC]=UAS-tdTom.S}2; P{y[+t7.7] w[+mC]=VT043140-GAL4.DBD}attP2 / P{y[+t7.7] w[+mC]=20XUAS-IVS-jGCaMP7f}VK00005
Fig. 5A-D – club neurons expressing tdTomato and GCaMP7f	w[1118]; P{y[+t7.7] w[+mC]= 50C12-p65ADZp}JK22C / P{w[+mC]=UAS-tdTom.S}2; P{y[+t7.7] w[+mC]=R84H05-GAL4.DBD}attP2 / P{y[+t7.7] w[+mC]=20XUAS-IVS-jGCaMP7f}VK00005
Fig. S1A - club	w[1118]; P{y[+t7.7] w[+mC]= 50C12-p65ADZp}JK22C / +; P{y[+t7.7] w[+mC]=R84H05-GAL4.DBD}attP2 / P{JFRC7-020XUAS-IVS-mCD8::GFP}attp2
Fig. S1A – hook extension	w[1118]; P{y[+t7.7] w[+mC]= VT018774-p65ADZ}attP40 / +; P{y[+t7.7] w[+mC]=VT040547-GAL4.DBD}attP2 / P{JFRC7-020XUAS-IVS-mCD8::GFP}attp2
Fig. S1A – hook flexion	w[1118]; P{y[+t7.7] w[+mC]= VT038873-p65ADZ}attP40 / +; P{y[+t7.7] w[+mC]=R32H08-GAL4.DBD}attP2 / P{JFRC7-020XUAS-IVS-mCD8::GFP}attp2
Fig. S1A – claw flexion	w[1118]; P{y[+t7.7] w[+mC]=R92D04-p65.AD}attP40 / + ; P{y[+t7.7] w[+mC]=VT043140-GAL4.DBD}attP2 / P{JFRC7-020XUAS-IVS-mCD8::GFP}attp2
Fig. S1A – claw extension	w[1118]; P{y[+t7.7] w[+mC]=R55C05-p65.AD}attP40 / + ; P{y[+t7.7] w[+mC]=VT017745-GAL4.DBD}attP2 / P{JFRC7-020XUAS-IVS-mCD8::GFP}attp2
Fig. S1B – club	P{w[+mC]=UAS-RedStinger}3, w[1118] / w[1118]; P{w[+m*]=lexAop-2xhrGFP.nls}2b / P{y[+t7.7] w[+mC]= 50C12-p65ADZp}JK22C; Mi{Trojan-LexA:QFAD.0}ChAT[MI04508-TLexA:QFAD.0] / P{y[+t7.7] w[+mC]=R84H05-GAL4.DBD}attP2
Fig. S1B – hook extension	P{w[+mC]=UAS-RedStinger}3, w[1118] / w[1118]; P{w[+m*]=lexAop-2xhrGFP.nls}2b / P{y[+t7.7] w[+mC]= VT018774-p65ADZ}attP40; Mi{Trojan-LexA:QFAD.0}ChAT[MI04508-TLexA:QFAD.0] / P{y[+t7.7] w[+mC]=VT040547-GAL4.DBD}attP2
Fig. S1B – hook flexion	P{w[+mC]=UAS-RedStinger}3, w[1118] / w[1118]; P{w[+m*]=lexAop-2xhrGFP.nls}2b / P{y[+t7.7] w[+mC]= VT038873-p65ADZ}attP40; Mi{Trojan-LexA:QFAD.0}ChAT[MI04508-TLexA:QFAD.0] / P{y[+t7.7] w[+mC]=R32H08-GAL4.DBD}attP2

Fig. S1B – claw flexion	P{w[+mC]=UAS-RedStinger}3, w[1118] / w[1118]; P{w[+m*]=lexAop-2xhrGFP.nls}2b / P{y[+t7.7] w[+mC]=R92D04-p65.AD}attP40; Mi{Trojan-LexA:QFAD.0}ChAT[MI04508-TLexA:QFAD.0] / P{y[+t7.7] w[+mC]=VT043140-GAL4.DBD}attP2
Fig. S1B – claw extension	P{w[+mC]=UAS-RedStinger}3, w[1118] / w[1118]; P{w[+m*]=lexAop-2xhrGFP.nls}2b / P{y[+t7.7] w[+mC]=R55C05-p65.AD}attP40; Mi{Trojan-LexA:QFAD.0}ChAT[MI04508-TLexA:QFAD.0] / P{y[+t7.7] w[+mC]=VT017745-GAL4.DBD}attP2
Fig. S2D-F – club	w[1118]; P{y[+t7.7] w[+mC]= 50C12-p65ADZp}JK22C / P{w[+mC]=UAS-tdTom.S}2; P{y[+t7.7] w[+mC]=R84H05-GAL4.DBD}attP2 / P{y[+t7.7] w[+mC]=20XUAS-IVS-jGCaMP7f}VK00005
Fig. S2F – hook flexion	w[1118]; P{y[+t7.7] w[+mC]= VT038873-p65ADZ}attP40 / P{w[+mC]=UAS-tdTom.S}2; P{y[+t7.7] w[+mC]=R32H08-GAL4.DBD}attP2 / P{y[+t7.7] w[+mC]=20XUAS-IVS-jGCaMP7f}VK00005
Fig. S2F – hook extension	w[1118]; P{y[+t7.7] w[+mC]= VT018774-p65ADZ}attP40 / P{w[+mC]=UAS-tdTom.S}2; P{y[+t7.7] w[+mC]=VT040547-GAL4.DBD}attP2 / P{y[+t7.7] w[+mC]=20XUAS-IVS-jGCaMP7f}VK00005
Fig. S2F – claw flexion	w[1118]; P{y[+t7.7] w[+mC]=R92D04-p65.AD}attP40 / P{w[+mC]=UAS-tdTom.S}2; P{y[+t7.7] w[+mC]=VT043140-GAL4.DBD}attP2 / P{y[+t7.7] w[+mC]=20XUAS-IVS-jGCaMP7f}VK00005
Fig. S2F – claw extension	w[1118]; P{y[+t7.7] w[+mC]=R55C05-p65.AD}attP40 / P{w[+mC]=UAS-tdTom.S}2; P{y[+t7.7] w[+mC]=VT017745-GAL4.DBD}attP2 / P{y[+t7.7] w[+mC]=20XUAS-IVS-jGCaMP7f}VK00005
Fig. S3 – iav expression	P{w[+mC]=UAS-RedStinger}3, w[1118] / w[*];P{w[+m*]=lexAop-2xhrGFP.nls}2b / +; Mi{Trojan-LexA:QFAD.0}ChAT[MI04508-TLexA:QFAD.0] / P{w[+mC]=iav-GAL4.K}3
Fig. S3 – nan expression	P{w[+mC]=UAS-RedStinger}3, w[1118] / w[*]; P{w[+mC]=nan-GAL4.K}2 / P{w[+m*]=lexAop-2xhrGFP.nls}2b ; Mi{Trojan-LexA:QFAD.0}ChAT[MI04508-TLexA:QFAD.0] / +
Fig. S3 – nompC expression	P{w[+mC]=UAS-RedStinger}3, w[1118] / y[1] w[*]; PBac{y[+mDint2] w[+mC]=nompC-GAL4.P}VK00014 / P{w[+m*]=lexAop-2xhrGFP.nls}2b ; Mi{Trojan-LexA:QFAD.0}ChAT[MI04508-TLexA:QFAD.0] / +
Fig. S3 – pain expression	P{w[+mC]=UAS-RedStinger}3, w[1118] / w[*]; P{w[+mW.hs]=GawB}pain[GAL4] / P{w[+m*]=lexAop-2xhrGFP.nls}2b ; Mi{Trojan-LexA:QFAD.0}ChAT[MI04508-TLexA:QFAD.0] / +
Fig. S3 – ppk1 expression	P{w[+mC]=UAS-RedStinger}3, w[1118] / y[1] w[*]; P{w[+m*]=lexAop-2xhrGFP.nls}2b / TI{GFP[3xP3.cLa]=CRIMIC.TG4.2}ppk[CR00622-TG4.2] ; Mi{Trojan-LexA:QFAD.0}ChAT[MI04508-TLexA:QFAD.0] / +
Fig. S3 – piezo expression	y[1] w[67c23] / y[1] w[*] ; Mi{PT-GFSTF.0}Piezo[MI04189-GFSTF.0] / + ; + / +
Fig. S3 – pzl expression	y[1] w[*] ; PBac{y[+mDint2] + / + ; PBac{13xLexAop2-CD4-tdTom}VK00033 P{GMR IAV-LexA}attP2 / Mi{y[+mDint2]=MIC}Pzl[MI02586] PBac{y[+mDint2]}
Fig. S3 – pyx expression	P{w[+mC]=UAS-RedStinger}3, w[1118] / y[1] w[*] ; P{w[+m*]=lexAop-2xhrGFP.nls}2b / + ; P{pyx-GAL4.pro17} / Mi{Trojan-LexA:QFAD.0}ChAT[MI04508-TLexA:QFAD.0]
Fig. S3 – stum expression	P{w[+mC]=UAS-RedStinger}3, w[1118] / w[*] ; P{w[+m*]=lexAop-2xhrGFP.nls}2b / P{w[+mC]=stum-GAL4.D}2 ; Mi{Trojan-LexA:QFAD.0}ChAT[MI04508-TLexA:QFAD.0] / +

Fig. S3 – Tmc expression	y[1] w[*] / y[1] w[*]; + / + ; Mi{PT-GFSTF.0}Tmc[MI02041-GFSTF.0] / +
Fig. S3 – Tmem63 expression	y[1] w[*]; tmem63-PGal4 / + ; PBac{13xLexAop2-CD4-tdTom}VK00033 P{GMR IAV-LexA}attP2 / P{pJFRC7-020XUAS-IVS-mCD8::GFP}attP2
Fig. S5C-D, G - claw cell and cap cells labeled with RFP and GFP	w[1118]; P{w[+mC]=nompA.GFP}5-3 / P{w[+mC]=UAS-RedStinger}4; P{y[+t7.7] w[+mC]=GMR73D10-GAL4}attP2
Fig. S6 – claw-flexion split-Gal4	w[1118]; P{y[+t7.7] w[+mC]=R92D04-p65.AD}attP40 / P{w[+mC]=UAS-tdTom.S}2; P{y[+t7.7] w[+mC]=VT043140-GAL4.DBD}attP2 / P{y[+t7.7] w[+mC]=20XUAS-IVS-jGCaMP7f}VK00005
Fig. S6 – claw-Gal4	w[1118]; P{w[+mC]=UAS-tdTom.S}2 / +; P{y[+t7.7] w[+mC]=GMR73D10-GAL4}attP2 / P{y[+t7.7] w[+mC]=20XUAS-IVS-jGCaMP7f}VK00005
Fig. S6 – claw extension split-Gal4	w[1118]; P{y[+t7.7] w[+mC]=R55C05-p65.AD}attP40 / P{w[+mC]=UAS-tdTom.S}2; P{y[+t7.7] w[+mC]=VT017745-GAL4.DBD}attP2 / P{y[+t7.7] w[+mC]=20XUAS-IVS-jGCaMP7f}VK00005
Fig. S8B-C – claw flexion	P{w[+mC]=UAS-RedStinger}3, w[1118] / w[1118]; P{y[+t7.7] w[+mC]=R92D04-p65.AD}attP40 / +; P{y[+t7.7] w[+mC]=VT043140-GAL4.DBD}attP2 / +
Fig. S8B-C – claw extension	P{w[+mC]=UAS-RedStinger}3, w[1118] / w[1118]; P{y[+t7.7] w[+mC]=R55C05-p65.AD}attP40 / +; P{y[+t7.7] w[+mC]=VT017745-GAL4.DBD}attP2 / +
Fig. S8B-C – hook extension	P{w[+mC]=UAS-RedStinger}3, w[1118] / w[1118]; P{y[+t7.7] w[+mC]= VT018774-p65ADZ}attP40 / +; P{y[+t7.7] w[+mC]=VT040547-GAL4.DBD}attP2 / +
Fig. S8B-C – hook flexion	P{w[+mC]=UAS-RedStinger}3, w[1118] / w[1118]; P{y[+t7.7] w[+mC]= VT038873-p65ADZ}attP40 / +; P{y[+t7.7] w[+mC]=R32H08-GAL4.DBD}attP2 / +
Fig. S8B-C – club	P{w[+mC]=UAS-RedStinger}3, w[1118] / w[1118]; P{y[+t7.7] w[+mC]= 50C12-p65ADZp}JK22C / +; P{y[+t7.7] w[+mC]=R84H05-GAL4.DBD}attP2 / +
Fig. S9 – club	w[1118]; P{y[+t7.7] w[+mC]= 50C12-p65ADZp}JK22C / P{w[+mC]=UAS-tdTom.S}2; P{y[+t7.7] w[+mC]=R84H05-GAL4.DBD}attP2 / P{y[+t7.7] w[+mC]=20XUAS-IVS-jGCaMP7f}VK00005

References

Agrawal, S., Dickinson, E.S., Sustar, A., Gurung, P., Shepherd, D., Truman, J.W., Tuthill, J.C., 2020. Central processing of leg proprioception in Drosophila. eLife 9, e60299. https://doi.org/10.7554/eLife.60299

Azevedo, A.W., Dickinson, E.S., Gurung, P., Venkatasubramanian, L., Mann, R.S., Tuthill, J.C., 2020. A size principle for recruitment of Drosophila leg motor neurons. eLife 9, e56754. https://doi.org/10.7554/eLife.56754

Bewick, G.S., Banks, R.W., 2021. Mechanotransduction channels in proprioceptive sensory nerve terminals: still an open question? Curr. Opin. Physiol. 20, 90–104. https://doi.org/10.1016/j.cophys.2020.11.007

Bogovic, J.A., Otsuna, H., Heinrich, L., Ito, M., Jeter, J., Meissner, G., Nern, A., Colonell, J., Malkesman, O., Ito, K., Saalfeld, S., 2020. An unbiased template of the Drosophila brain and ventral nerve cord. PLOS ONE 15, e0236495. https://doi.org/10.1371/journal.pone.0236495

Chen, C., Agrawal, S., Mark, B., Mamiya, A., Sustar, A., Phelps, J.S., Lee, W.-C.A., Dickson, B.J., Card, G.M., Tuthill, J.C., 2021. Functional architecture of neural circuits for leg proprioception in Drosophila. Curr. Biol. S0960982221012756. https://doi.org/10.1016/j.cub.2021.09.035

Euler, T., Hausselt, S.E., Margolis, D.J., Breuninger, T., Castell, X., Detwiler, P.B., Denk, W., 2009. Eyecup scope—optical recordings of light stimulus-evoked fluorescence signals in the retina. Pflüg. Arch. - Eur. J. Physiol. 457, 1393–1414. https://doi.org/10.1007/s00424-008-0603-5

Fettiplace, R., Fuchs, P.A., 1999. Mechanisms of hair cell tuning. Annu. Rev. Physiol. 61, 809–834. https://doi.org/10.1146/annurev.physiol.61.1.809

Field, L.H., 1991. Mechanism for range fractionation in chordotonal organs of Locusta migratoria (L) and Valanga sp. (Orthoptera : Acrididae). Int. J. Insect Morphol. Embryol. 20, 25–39. https://doi.org/10.1016/0020-7322(91)90025-5

Field, L.H., Matheson, T., 1998. Chordotonal organs of insects, in: Advances in Insect Physiology. Elsevier, pp. 1–228.

Frantsevich, L., Shumakova, I., Gladun, D., 2019. Mechanical and optical properties of the femoral chordotonal organ in beetles (Coleoptera). J. Exp. Biol. 222. https://doi.org/10.1242/jeb.203968

Gosline, J., Lillie, M., Carrington, E., Guerette, P., Ortlepp, C., Savage, K., 2002. Elastic Proteins: Biological Roles and Mechanical Properties. Philos. Trans. Biol. Sci. 357, 121–132.

Graber, V., 1881. Die chordotonalen Sinnesorgane und das Gehör der Insecten. Arch. Für Mikrosk. Anat. 20, 506–640. https://doi.org/10.1007/BF02952659

Guizar-Sicairos, M., Thurman, S.T., Fienup, J.R., 2008. Efficient subpixel image registration algorithms. Opt. Lett. 33, 156. https://doi.org/10.1364/OL.33.000156

Haralick, R.M., Shapiro, L.G., 1992. Computer and robot vision [WWW Document]. CERN Doc. Serv. URL https://cds.cern.ch/record/338554 (accessed 3.18.20).

Hehlert, P., Zhang, W., Göpfert, M.C., 2021. Drosophila Mechanosensory Transduction. Trends Neurosci. 44, 323–335. https://doi.org/10.1016/j.tins.2020.11.001

Hummel, J., Kössl, M., Nowotny, M., 2017. Morphological basis for a tonotopic design of an insect ear. J. Comp. Neurol. 525, 2443–2455. https://doi.org/10.1002/cne.24218

Jefferis, G.S.X.E., Potter, C.J., Chan, A.M., Marin, E.C., Rohlfing, T., Maurer, C.R., Luo, L., 2007. Comprehensive Maps of Drosophila Higher Olfactory Centers: Spatially Segregated Fruit and Pheromone Representation. Cell 128, 1187–1203. https://doi.org/10.1016/j.cell.2007.01.040

Jenett, A., Rubin, G.M., Ngo, T.-T.B., Shepherd, D., Murphy, C., Dionne, H., Pfeiffer, B.D., Cavallaro, A., Hall, D., Jeter, J., Iyer, N., Fetter, D., Hausenfluck, J.H., Peng, H., Trautman, E.T., Svirskas, R.R., Myers, E.W., Iwinski, Z.R., Aso, Y., DePasquale, G.M., Enos, A., Hulamm, P., Lam, S.C.B., Li, H.-H., Laverty, T.R., Long, F., Qu, L., Murphy, S.D., Rokicki, K., Safford, T., Shaw, K., Simpson, J.H., Sowell, A., Tae, S., Yu, Y., Zugates, C.T., 2012. A GAL4-driver line resource for Drosophila neurobiology. Cell Rep. 2, 991–1001. https://doi.org/10.1016/j.celrep.2012.09.011

Karashchuk, P., Rupp, K.L., Dickinson, E.S., Walling-Bell, S., Sanders, E., Azim, E., Brunton, B.W., Tuthill, J.C., 2021. Anipose: A toolkit for robust markerless 3D pose estimation. Cell Rep. 36, 109730. https://doi.org/10.1016/j.celrep.2021.109730

Krishnan, A., Sane, S.P., 2015. Chapter Three - Antennal Mechanosensors and Their Evolutionary Antecedents, in: Jurenka, R. (Ed.), Advances in Insect Physiology. Academic Press, pp. 59–99. https://doi.org/10.1016/bs.aiip.2015.06.003

Kuan, A.T., Phelps, J.S., Thomas, L.A., Nguyen, T.M., Han, J., Chen, C.-L., Azevedo, A.W., Tuthill, J.C., Funke, J., Cloetens, P., Pacureanu, A., Lee, W.-C.A., 2020. Dense neuronal reconstruction through X-ray holographic nano-tomography. Nat. Neurosci. 1–7. https://doi.org/10.1038/s41593-020-0704-9

Levental, I., Georges, P.C., Janmey, P.A., 2007. Soft biological materials and their impact on cell function. Soft Matter 3, 299–306. https://doi.org/10.1039/B610522J

Li, H., Janssens, J., De Waegeneer, M., Kolluru, S.S., Davie, K., Gardeux, V., Saelens, W., David, F.P.A., Brbić, M., Spanier, K., Leskovec, J., McLaughlin, C.N., Xie, Q., Jones, R.C., Brueckner, K., Shim, J., Tattikota, S.G., Schnorrer, F., Rust, K., Nystul, T.G., Carvalho-Santos, Z., Ribeiro, C., Pal, S., Mahadevaraju, S., Przytycka, T.M., Allen, A.M., Goodwin, S.F., Berry, C.W., Fuller, M.T., White-Cooper, H., Matunis, E.L., DiNardo, S., Galenza, A., O'Brien, L.E., Dow, J.A.T., FCA Consortium, Jasper, H., Oliver, B., Perrimon, N., Deplancke, B., Quake, S.R., Luo, L., Aerts, S., 2022. Fly Cell Atlas: A single-nucleus transcriptomic atlas of the adult fruit fly. Science 375, eabk2432. https://doi.org/10.1126/science.abk2432

Macefield, V.G., Knellwolf, T.P., 2018. Functional properties of human muscle spindles. J. Neurophysiol. 120, 452–467. https://doi.org/10.1152/jn.00071.2018

Mamiya, A., Gurung, P., Tuthill, J.C., 2018. Neural Coding of Leg Proprioception in Drosophila. Neuron 100, 636-650.e6. https://doi.org/10.1016/j.neuron.2018.09.009

Matheson, T., 1992. Range fractionation in the locust metathoracic femoral chordotonal organ. J. Comp. Physiol. A 170, 509–520.

Mathis, A., Mamidanna, P., Cury, K.M., Abe, T., Murthy, V.N., Mathis, M.W., Bethge, M., 2018. DeepLabCut: markerless pose estimation of user-defined body parts with deep learning. Nat. Neurosci. 21, 1281–1289. https://doi.org/10.1038/s41593-018-0209-y

McKelvey, E.G.Z., Gyles, J.P., Michie, K., Barquín Pancorbo, V., Sober, L., Kruszewski, L.E., Chan, A., Fabre, C.C.G., 2021. Drosophila females receive male substrate-borne signals through specific leg neurons during courtship. Curr. Biol. https://doi.org/10.1016/j.cub.2021.06.002

Nagel, M., Chesler, A.T., 2022. PIEZO2 ion channels in proprioception. Curr. Opin. Neurobiol. 75, 102572. https://doi.org/10.1016/j.conb.2022.102572

Nishino, H., Sakai, M., 1997. Three neural groups in the femoral chordotonal organ of the cricket Gryllus bimaculatus: central projections and soma arrangement and displacement during joint flexion. J. Exp. Biol. 200, 2583–2595. https://doi.org/10.1242/jeb.200.20.2583

Oldfield, B.P., 1982. Tonotopic organisation of auditory receptors in tettigoniidae (Orthoptera: Ensifera). J. Comp. Physiol. 147, 461–469. https://doi.org/10.1007/BF00612011

Phelps, J.S., Hildebrand, D.G.C., Graham, B.J., Kuan, A.T., Thomas, L.A., Nguyen, T.M., Buhmann, J., Azevedo, A.W., Sustar, A., Agrawal, S., Liu, M., Shanny, B.L., Funke, J., Tuthill, J.C., Lee, W.-C.A., 2021. Reconstruction of motor control circuits in adult Drosophila using automated transmission electron microscopy. Cell 184, 759-774.e18. https://doi.org/10.1016/j.cell.2020.12.013

Pologruto, T.A., Sabatini, B.L., Svoboda, K., 2003. ScanImage: Flexible software for operating laser scanning microscopes. Biomed. Eng. OnLine 2, 13. https://doi.org/10.1186/1475-925X-2-13

Rydholm, S., Zwartz, G., Kowalewski, J.M., Kamali-Zare, P., Frisk, T., Brismar, H., 2010. Mechanical properties of primary cilia regulate the response to fluid flow. Am. J. Physiol.-Ren. Physiol. 298, F1096–F1102. https://doi.org/10.1152/ajprenal.00657.2009

Saalfeld, S., Cardona, A., Hartenstein, V., Tomančák, P., 2009. CATMAID: collaborative annotation toolkit for massive amounts of image data. Bioinformatics 25, 1984–1986. https://doi.org/10.1093/bioinformatics/btp266

Schlegel, P., Texada, M.J., Miroschnikow, A., Schoofs, A., Hückesfeld, S., Peters, M., Schneider-Mizell, C.M., Lacin, H., Li, F., Fetter, R.D., Truman, J.W., Cardona, A., Pankratz, M.J., 2016. Synaptic transmission parallels neuromodulation in a central food-intake circuit. eLife 5, e16799. https://doi.org/10.7554/eLife.16799

Schneider-Mizell, C.M., Gerhard, S., Longair, M., Kazimiers, T., Li, F., Zwart, M.F., Champion, A., Midgley, F.M., Fetter, R.D., Saalfeld, S., Cardona, A., 2016. Quantitative neuroanatomy for connectomics in Drosophila. eLife 5, e12059. https://doi.org/10.7554/eLife.12059

Shanbhag, S.R., Singh, K., Naresh Singh, R., 1992. Ultrastructure of the femoral chordotonal organs and their novel synaptic organization in the legs of Drosophila melanogaster Meigen (Diptera : Drosophilidae). Int. J. Insect Morphol. Embryol. 21, 311–322. https://doi.org/10.1016/0020-7322(92)90026-J

Tuthill, J.C., Azim, E., 2018. Proprioception. Curr. Biol. 28, R194–R203. https://doi.org/10.1016/j.cub.2018.01.064

Vincent, J.F.V., Wegst, U.G.K., 2004. Design and mechanical properties of insect cuticle. Arthropod Struct. Dev. 33, 187–199. https://doi.org/10.1016/j.asd.2004.05.006